Global Biogeochemical Cycles®

RESEARCH ARTICLE
10.1029/2022GB007667

Special Section:
The U.S. GEOTRACES Pacific Meridional Transect (GP15)

A North Pacific Meridional Section (U.S. GEOTRACES GP15) of Helium Isotopes and Noble Gases I: Deep Water Distributions

William J. Jenkins[1], Scott C. Doney[2], Alan M. Seltzer[1], Christopher R. German[3], Dempsey E. Lott III[1], and Kevin L. Cahill[1]

[1]Department of Marine Chemistry and Geochemistry, Woods Hole Oceanographic Institution, Woods Hole, MA, USA, [2]Department of Environmental Change, University of Virginia, Charlottesville, VA, USA, [3]Department of Geology and Geophysics, Woods Hole Oceanographic Institution, Woods Hole, MA, USA

Key Points:

- Noble gases constrain the rate of basal melting of Antarctic Glaciers
- Noble gases allow us to constrain the isotopic composition of helium being added to deep waters
- The distribution of helium isotopes mirrors important geological and geophysical processes in the Pacific

Supporting Information:

Supporting Information may be found in the online version of this article.

Correspondence to:

W. J. Jenkins,
wjenkins@whoi.edu

Citation:

Jenkins, W. J., Doney, S. C., Seltzer, A. M., German, C. R., Lott, D. E. III., & Cahill, K. L. (2023). A North Pacific meridional section (U.S. GEOTRACES GP15) of helium isotopes and noble gases I: Deep water distributions. *Global Biogeochemical Cycles*, *37*, e2022GB007667. https://doi.org/10.1029/2022GB007667

Received 3 DEC 2022
Accepted 11 APR 2023

Author Contributions:

Conceptualization: William J. Jenkins, Scott C. Doney
Formal analysis: William J. Jenkins
Funding acquisition: Scott C. Doney, Christopher R. German
Methodology: William J. Jenkins, Dempsey E. Lott III
Project Administration: William J. Jenkins, Scott C. Doney
Resources: William J. Jenkins, Dempsey E. Lott III, Kevin L. Cahill

Abstract The noble gas signature of incoming Pacific Bottom Water (PBW), when compared to North Atlantic Deep Water, indicates the addition of 450 ± 70 GT a^{-1} glacial melt water to form AABW and subsequently PBW. The downstream evolution of this signature between the southern (20°S to equator) and northern (25°–45°N) bottom waters indicates a decrease in sea level pressure around Antarctica over the past two millennia. Vertical profiles of noble gases in the deep Pacific show exponential relationships with depth with scale heights identical to temperature and salinity. Unlike the other noble gases, helium isotopes show evidence of mid-depth injection of non-atmospheric helium. Using observed deviations from exponential behavior, we quantify its magnitude and isotope ratio. There is a clear latitude trend in the isotope ratio of this added helium that decreases from a high exceeding 9 R_A (atmospheric $^3He/^4He$ ratio) in the south to around 8 R_A near the equator. North of 30–40°N, it systematically decreases northward to a low of ~2 R_A north of 50°N. This decline results from a combination of northward decline in seafloor spreading, release of radiogenic helium from increased sediment thickness, and the possible emission of radiogenic helium through cold seeps along the Alaskan and North American margins. Finally, we derive an improved method of computing the excess helium isotope concentrations and that the distributions of bottom water $^3He_{XS}/^4He_{XS}$ are consistent with what is known about bottom water flow patterns and the input of low $^3He/^4He$ sedimentary helium.

Plain Language Summary Dissolved noble gases, because they are inert and span a range of physical characteristics, uniquely record conditions at the sea surface when water masses are formed and sink from polar regions to fill the abyssal ocean. These signatures can be used not only to deduce past changes in sea level pressure and rates of glacial melting but also to disentangle air-sea exchange and in situ physical processes that affect all gases from subsurface external sources that are unique for helium isotopes. The distribution of helium isotopes in the deep ocean can be used to constrain the patterns and magnitudes of hydrothermal sources at the sea floor as well as the input of sedimentary radiogenic helium and cold seeps to Pacific bottom water. We use these tools to study the various sources of helium isotopes in the abyssal Northeast Pacific.

1. Introduction

The global marine cycles of many elements are significantly affected by sea-floor hydrothermal processes (Edmond et al., 1979; Elderfield & Schultz, 1996). This is particularly true of the lightest noble gas, helium. Since helium isotopes are stable and inert in the deep ocean, they can be used as tracers of this hydrothermal influence. Recent estimates of the global marine hydrothermal ^3He flux (Bianchi et al., 2010; DeVries & Holzer, 2019; Schlitzer, 2016) have converged to ~550 mol a^{-1} (Jenkins, 2020), which allows one to estimate the hydrothermal flux of other elements given observation of their ratio to this "gauge isotope" (e.g., Jenkins et al., 1978; Resing et al., 2015). On more local/regional scales, tracking the ratios of these non-conservative elements to ^3He also provides information on dilution and in situ biogeochemical processes that serve to alter their abundances. In some cases, regional scale flux estimates can be made (e.g., Jenkins et al., 2020).

In addition, the abundances of the other stable noble gases (Ne, Ar, Kr, and Xe) dissolved in seawater provide important clues about ocean ventilation (Hamme et al., 2019), ice-seawater interaction (Loose & Jenkins, 2014), mixing (Ito & Deutsch, 2006), and even past changes in sea-level pressure (Jenkins, Doney, et al., 2023; Jenkins, Seltzer, et al., 2023). These elements have differing physical properties, including solubility (both magnitude

Software: William J. Jenkins
Validation: William J. Jenkins
Visualization: William J. Jenkins
Writing – original draft: William J. Jenkins
Writing – review & editing: Scott C. Doney, Alan M. Seltzer, Christopher R. German

and temperature dependence), atomic radius, and molecular diffusivity that span roughly an order of magnitude. Thus, they provide unique and preserved fingerprints of the many physical processes that also influence climatically and biologically important gases such as CO_2 and O_2.

In this, the first of two papers, we discuss the deep-water distributions of helium isotopes and noble gases along north-south section in the middle of the Northeast Pacific Basin. In the second, following paper, we interpret the shallow distribution of helium isotopes, their relationship to bomb tritium, noble gases, and their ocean-atmospheric fluxes (Jenkins, Doney, et al., 2023; Jenkins, Seltzer, et al., 2023).

2. Methods

We report here (and in the accompanying paper) results from two occupations along a meridional section at ~152°W in the middle of the North Pacific from ~20°S to the Alaskan coast. The earlier GOSHIP cruise was occupied in spring-summer of 2015 and concentrated on the upper 2 km of the water column. This involved a total of 364 helium isotope measurements, 142 noble gas measurements, and 417 tritium determinations at a total of 28 locations. The later GEOTRACES GP15 cruise was occupied in the late autumn of 2018 and sampled the full water column. This included 945 helium isotope and noble gas measurements at 34 stations.

Water samples were collected for helium isotope and noble gas measurement using the crimped copper tube method pioneered by Young and Lupton (Young & Lupton, 1983), whereby water from the Niskin bottle (mounted on a CTD rosette) is gravity transferred via plastic tubing to a 76 cm length of 1.6 cm O.D. copper tubing. The copper tubing is crimped in three places to produce a pair of ~45 g duplicate water samples in hermetically sealed copper capsules. On shore, the water samples are quantitatively gas extracted and mass spectrometrically measured for helium isotope ratios and noble gas abundances using the methods described in Jenkins, Lott, and Cahill (2019, and references therein). Based on replicate analyses and inter-comparison of independent standards, the results are accurate to 0.15% (1 standard deviation) for the helium isotope ratio anomaly relative to atmosphere, as defined by

$$\delta^3\mathrm{He} = \left(\frac{\left({}^3\mathrm{He}/{}^4\mathrm{He}\right)_X}{\left({}^3\mathrm{He}/{}^4\mathrm{He}\right)_A} - 1 \right) \times 100\% \quad (1)$$

where the subscripts X and A refer to the sample and atmospheric standard respectively. The helium isotope ratios were corrected for a modest, empirically determined, analytical sample-size-dependence, and for a small in-storage tritium decay effect (negligible in the deep waters and described more thoroughly in the companion paper (Jenkins, Doney, et al., 2023; Jenkins, Seltzer, et al., 2023)). The noble gas concentrations were measured on the same gas samples to an accuracy of better than 0.2% (one standard deviation) by a combination of peak-height manometry (He, Ne, and Ar) and ratiometric isotope dilution (Kr and Xe) methods described elsewhere (Jenkins, Lott, & Cahill 2019; Stanley, Baschek, et al., 2009). Concentration results are reported here in terms of the saturation anomaly, which is defined as the percent deviation of the measured concentration (C) of a gas from solubility equilibrium (C^*) at precisely one atm pressure and at the salinity and potential temperature of the sample, as defined (for helium, e.g.,) by

$$\Delta\mathrm{He} = \left(\frac{C(\mathrm{He})}{C^*(\mathrm{He})} - 1 \right) \times 100\% \quad (2)$$

where the solubility equilibrium concentrations were determined using the same standards and analytical methods and equipment (Jenkins, Lott, and Cahill 2019). The data have been archived at both the BCO-DMO (Jenkins & German, 2021a, 2021b) (Jenkins & German, 2021a, 2021b; Jenkins et al., 2022a, 2022b) and CCHDO repositories.

3. Results

Figures 1a—d are four section plots for the measured noble gases (Ne, Ar, Kr, and Xe), excluding He. The sections are rendered from south (left) to north (right) with the seafloor at bottom in dark gray and the equator as a light gray vertical line. Each section plot contains two panels consisting of a depth panel (from 800 to 6,000 m, lower) and a neutral density panel (from γ^n = 27. 5 to 28.15 kg m^{-3}, upper). The choice of the neutral density (Jackett & McDougall, 1997) and depth ranges was made to encompass the extent of the deep overturning circulation

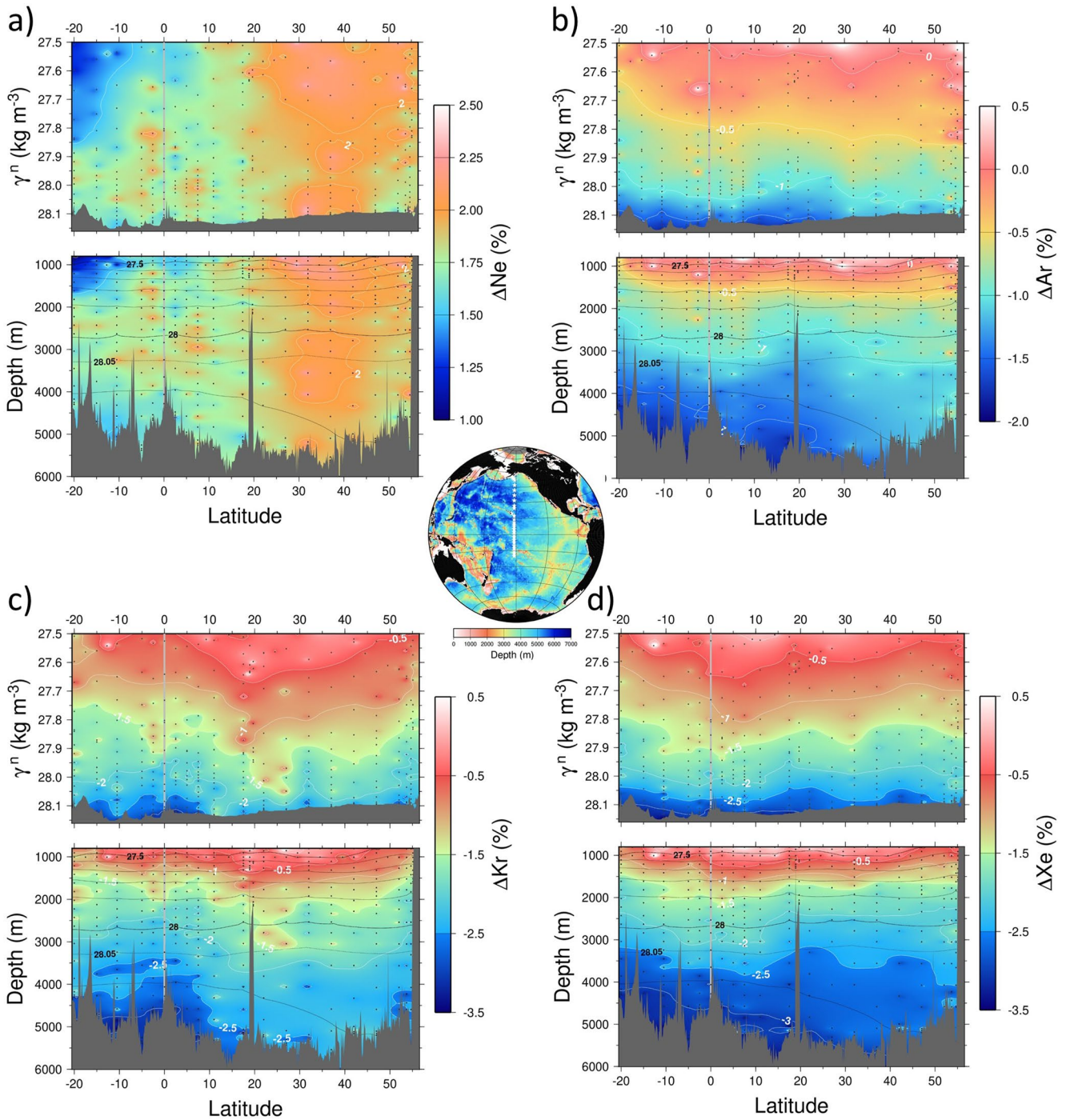

Figure 1. Contoured sections of the saturation anomalies of (a) Ne, (b) Ar, (c) Kr, and (d) Xe along ~152°W from 20°S (left) to 56.5°N (right). The vertical axis in the upper panel is neutral density anomaly and in the lower panel is the depth. South is on the left for each section, and station locations are indicated by small white stars in the inset topographic map.

(below ~1,000 m depth, see e.g., Bryden et al., 1991; MacDonald et al., 2009; Wijffels et al., 1996, 2001). White contour lines are used along with a color scheme that is unique to each gas (except that Kr and Xe are identical). Sample locations are indicated by black dots on the plots, and neutral density anomaly is contoured in black on the depth plots.

Although all four gases (Ne, Ar, Kr, and Xe) show evidence of younger, incoming bottom water from the south, the distributions reflect the overall circulation pattern in differing ways. The ΔNe distribution is unique in that

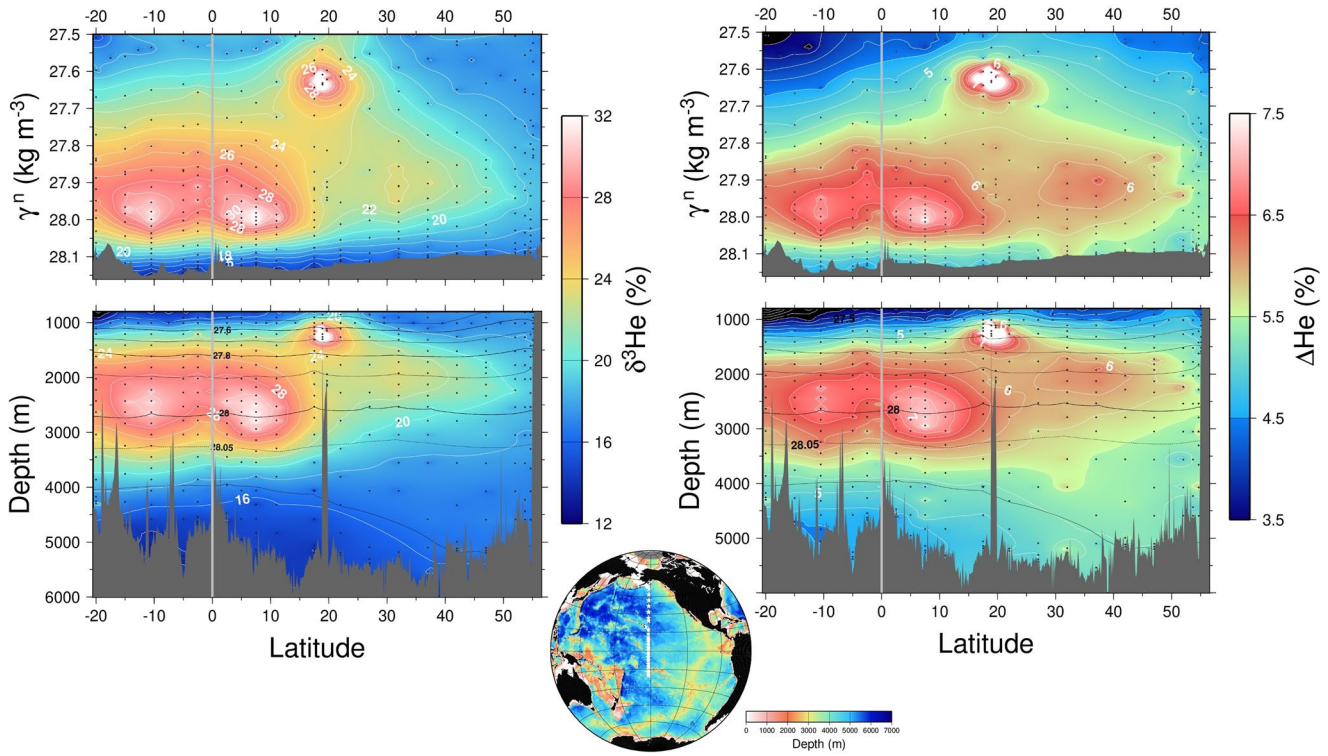

Figure 2. Contoured sections of (a) the helium isotope ratio anomaly and (b) the He saturation anomaly along ~152°W from 20°S (left) to 56.5°N (right). The vertical axis in the upper panel is neutral density anomaly and in the lower panel is the depth.

it has positive saturation anomalies (the other gas saturation anomalies are negative), shows much less variation (note the color scale range for ΔNe is only 1.5% while for ΔAr it is 2.5% and ΔKr and ΔXe are 4%), and exhibits unique features. For example, ΔNe has broadly distributed maximum north of about 20°N, where values exceed 2% at mid-depths. Although this maximum appears at first to be a single feature, it consists of least three vertical maxima, separated by relative minima at ~2,200 and ~1,500 m depths (γ^N ~28.0 and ~27.8 kg m^{-3}). In contrast, the heavier noble gases are generally undersaturated in the deep waters, becoming increasingly negative from Ar to Kr to Xe. The contrast is most pronounced for Xe. The incoming bottom water ranges from ΔAr ~ −1.5% to ΔXe ~ −3.5%, but with all three gas saturation anomalies trending toward positive values in shallower waters. The overall deep-water patterns are qualitatively similar to that described earlier for a station near Hawaii, which were attributed to air-sea disequilibrium during deep-water formation (Hamme & Severinghaus, 2007). The behavioral contrast between Ne and the other gases reflects its much lower solubility (hence sensitivity to bubble injection) and its weaker dependence on temperature. In addition to mixing and air-sea exchange processes during water mass formation, interaction with the massive grounded ice shelves around Antarctica is another mechanism affecting noble gas saturation anomalies (Beaird et al., 2015; Loose & Jenkins, 2014; Loose et al., 2016). The effects of this last interaction range from an enhancement of the lighter noble gases through to a decrease in saturation anomalies of the heavier gases.

If there were no non-atmospheric inputs of helium into the ocean, the ΔHe distribution would resemble that of ΔNe (Figure 1a) due to its similar physical properties. Like the heavier noble gases, the ΔHe distribution does reflect the bottom water invasion, but in contrast, δ^3He (Figure 2a) and ΔHe (Figure 2b) exhibit a strikingly different mid-depth pattern. This difference, of course, is the imprint of the long-documented hydrothermal injection of these isotopes into Pacific Deep water (Clarke et al., 1969; Jenkins et al., 1978; Lupton & Craig, 1981). The correspondence between the two helium anomalies is striking. They exhibit similar structure because the isotope ratios (^{3}He/^{4}He) of the hydrothermal end-members, although high relative to the atmosphere, are not infinite. That is, a detectable amount of mantle/hydrothermal ^{4}He is also injected into the water column along with the ^{3}He. There are four major structural features immediately evident. The first two appear at γ^n ~ 27.98–28.0 kg m^{-3} or 2,500–2,600 m depth approximately 10° of latitude on either side of the equator. These are the imprint of

Table 1
Average Saturation Anomalies (in %) for PBW and NADW, Their Changes, and Uncertainties

Gas	PBW	σ_{AABW}	NADW	σ_{NADW}	PBW—NADW	σ_{Diff}
ΔNe	1.66	0.02	0.90	0.04	0.76	0.04
ΔAr	−1.62	0.03	−1.65	0.07	0.03	0.08
ΔKr	−2.77	0.04	−2.51	0.08	−0.26	0.09
ΔXe	−3.07	0.04	−2.79	0.08	−0.28	0.09

hydrothermal emanations from the East Pacific Rise (EPR), where buoyancy injection drives basin-wide deep anticyclonic gyres (Stommel, 1982), leading to two westward flowing plumes on either side of the equator (Jenkins et al., 2018; Lupton & Craig, 1981; Wijffels et al., 1996). A third feature appears at a slightly shallower depth (∼2,200 m) and lighter density (∼27.9 kg m^{-3}) between 30 and 40°N. This is likely a signature of the westward flow of Juan de Fuca hydrothermal emissions (Butterfield et al., 1990; Lupton et al., 1999). Finally, there is a shallow feature at ∼1,100 m depth (27.62 kg m^{-3}) near 19°N associated with the Kama'ehuakanaloa (previously known as Loihi) Seamount (Jenkins et al., 2020). While the first three have a common origin, namely high temperature hydrothermal emanations from the East Pacific Rise crest, the relatively shallow Kama'ehuakanaloa feature arises from relatively low temperature hydrothermal activity on an intraplate volcanic edifice fed by a mantle plume. Examination of the helium isotope systematics for the three "ridge crest" features reveal $^3He/^4He$ ratios near the terrestrial asthenospheric value of ∼8–10 R_A (where R_A is the atmospheric ratio (1.384e−6, Clarke et al., 1976)), while the shallow Kama'ehuakanaloa feature exceeds 27 R_A, reflecting deeper, more primitive volatile origins (Jenkins et al., 2020). Water column anomalies at a depth of 1,100 m are observed to extend eastward to the North American coast (Lupton, 1998a), which allows a robust estimate of flux of ^3He from this edifice, namely 10 mol a^{-1}, which corresponds to roughly 2% of the global terrestrial hydrothermal ^3He flux (Jenkins et al., 2020).

4. Discussion

Previously, we have used a simple heuristic relationship that utilized the observed concentrations of Ne, which is the noble gas most similar to He in physical characteristics and has no in situ sources or sinks in the deep ocean, to estimate the atmospheric contribution to the observed helium abundance and isotopic composition (see Jenkins et al., 2018, and a later section). However, as will become evident, this simple approach may neglect other important contributions to the non-hydrothermal contributions to ΔHe. In order to properly account for those isotopes, we need to consider the distributions of the other noble gases. In doing this, however, we will find other useful constraints on oceanographic processes. We begin by describing and rationalizing the noble gas patterns along the trajectory of the meridional overturning circulation (MOC), starting with the incoming bottom water, its transit from the South Pacific into the abyssal Northeast Pacific, and its upwelling and subsequent southward return at depths below about 2,200–2,500 m. As such, we are following the Pacific bottom- and deep-water overturning route described by Kuhlbrodt, Talley, Holzer, and others (Holzer et al., 2021; Kuhlbrodt et al., 2007; Talley, 2013).

5. Bottom Waters

We first examine the average saturation anomalies of incoming PBW (Pacific Bottom Water) for Ne, Ar, Kr, and Xe by averaging all measurements below the $\gamma^N = 28.05$ kg m^{-3} isoneutral horizon (see dashed black lines in Figures 1 and 2) between the southernmost extent of this section (∼20°S) and the equator. Based on the noble gas and helium isotope distributions, we use this isoneutral to demarcate the boundary between incoming bottom water and returning deep water. It is slightly shallower than the $\gamma^N = 28.1$ kg m^{-3} isoneutral horizon used by Holzer et al. (2021) but the choice doesnt significantly affect our analysis. The averages are summarized in Table 1 (columns 2 and 3), along with their uncertainties, as defined by the standard error of the mean ($N = 75$ for each gas). This water mass is essentially derived from water mass formation processes near Antarctica (Gebbie & Huybers, 2010; Gordon, 2019; Talley, 2013), including the addition of glacial melt water created by basal melting induced by contact between relatively warm deep water and grounded glaciers (Biddle et al., 2019; Holland & Jenkins, 2008; Jacobs et al., 1996). This cold dense water further mixes with Circumpolar Deep Water and modified North Atlantic Deep Water as it moves toward the Indian and Pacific Oceans. For comparison, we determined the mean characteristics of North Atlantic Deep Water (NADW) based on observations of that water mass in the subtropical and subpolar North Atlantic (columns 4 and 5, see Supporting Information S1) and compute the differences between those water masses and their propagated uncertainties (columns 6 and 7).

The pattern of those changes is distinct and unique. Note that the most affected gas is Ne, which shows a 0.76% ± 0.04% increase from NADW to PBW. Inasmuch as noble gases are chemically and biologically inert,

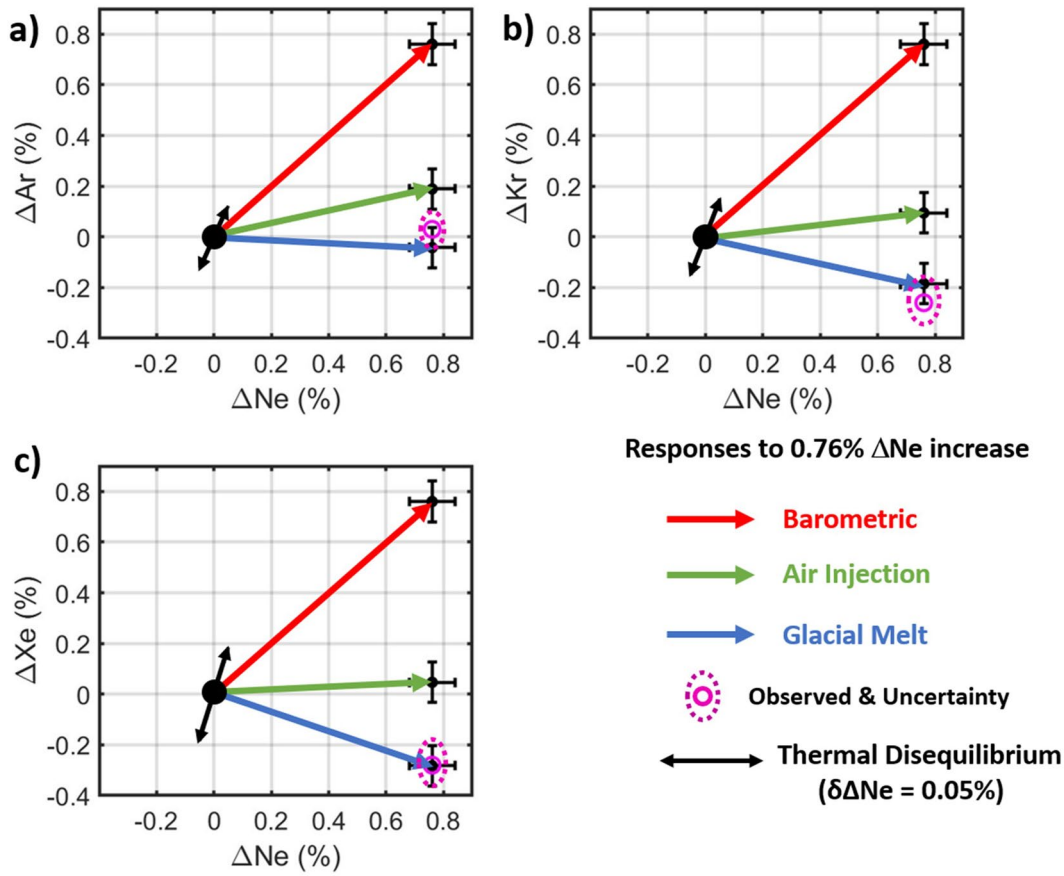

Figure 3. Schematic response in the heavy noble gas saturation anomalies to an increase of 0.76% in ΔNe by various processes designated as different colored vectors (see text). The actual changes between NADW and AABW are shown as the magenta circles with the uncertainty expressed by the dotted ellipse.

there are only a limited number of processes that can cause these changes. Figure 3 is a schematic of the calculated responses of the other three noble gases associated with those candidate processes that are consistent with a 0.76% increase in ΔNe. There are three plots for each of (a) ΔAr, (b) ΔKr, and (c) ΔXe, projecting possible changes in those gases based on the observed change in ΔNe. An increase in sea level pressure (red vectors) affects all gases proportionately since they must obey Henry's Law (Henry, 1803). Changes due to larger amounts of air injection (bubble entrapment and dissolution due to wave action at the sea surface) are represented by the green arrows and affect the more soluble gases correspondingly less (Stanley, Jenkins, et al., 2009). The third candidate process is the addition of glacial melt water (GMW) due to basal melting of grounded glaciers around the coast of Antarctica (blue vector). Here again, the lighter, less soluble noble gases are most affected due to the inclusion of glacial air bubbles (which increases saturation), but for the more soluble gases, this process is actually reversed by the extraction of latent heat from seawater due to ice melting, which lowers seawater temperature and consequently the saturation anomalies (i.e., induces greater undersaturation) for the more soluble gases (Loose & Jenkins, 2014) due to their steeper solubility dependence on temperature (Jenkins, Lott, & Cahill 2019). Fourth, the solid black vectors in the graphs indicate the expected change due to thermal disequilibrium associated with a 0.05% change in ΔNe. Finally, although significant enhancement of noble gas saturation anomalies due to diapycnal mixing has been identified in the main thermocline (Emerson et al., 2012; Ito & Deutsch, 2006; Ito et al., 2007), the magnitude of this effect depends on spatial curvature in temperature, which is characteristically weak in deep and bottom waters. Using transport matrix methods (Khatiwala, 2007) from an intermediate complexity earth system climate model (Mengis et al., 2020; Seltzer et al., 2023) for the deep Pacific, we estimate the maximum enhancement of ΔNe due to diapycnal mixing to be less than a tenth of this value (~0.004%), so the largest enhancement for the most susceptible noble gas (Xe) would be less than 0.02%. Hence, we conclude that diapycnal mixing makes no significant contribution to the observations. In summary,

Table 2
Average Saturation Anomalies (in %) for PBW and NPBW, Their Changes, and Uncertainties

Gas	PBW	σ_{AABW}	NPBW	σ_{NPBW}	NPBW—PBW	σ_{Diff}
ΔNe	1.66	0.02	2.01	0.05	0.35	0.05
ΔAr	−1.62	0.03	−1.23	0.04	0.39	0.05
ΔKr	−2.77	0.04	−2.31	0.08	0.47	0.12
ΔXe	−3.07	0.04	−2.67	0.06	0.41	0.08

it is clear that the observed differences (the magenta circles and dotted black ellipses in the plots) are only consistent with this last process, where all three gases are within errors of the GMW projection.

When NADW enters the Southern Ocean, it upwells, mixing with Circumpolar Deep Water and the combined water masses seed the formation of AABW around several regions (e.g., Weddell, Ross, and Amundsen Seas) near Antarctica (e.g., Orsi et al., 2001; Talley, 2013). This involves a combination of air-sea exchange (largely in polynyas (Gordon, 2019)) and the addition of GMW from basal melting of grounded ice shelves (Huhn et al., 2008; Jacobs et al., 1996; Loose et al., 2016). Given NADW formation rates (Gordon, 2019; Talley, 2013) of $18 \pm 2 \times 10^6$ m^3 s^{-1}, and estimates of AABW formation rates (Gordon, 2019; Orsi et al., 2002) ranging from 14.5 to 17.5×10^6 m^3 s^{-1} we can use the relationship between glacial melting and noble gas saturation anomalies (Loose & Jenkins, 2014) to estimate a GMW production of $4.5 \pm 0.7 \times 10^{11}$ m^3 a^{-1}, equivalent to an Antarctic basal melt rate of 450 ± 70 GT a^{-1}. This calculation assumes that any air-sea exchange during the formation of AABW will have a noble gas signature similar to that of NADW formation, which is a reasonable assumption since similar processes (wind forcing, deep convection) occur in both regions.

Recent estimates of Antarctic basal melt rates (Adusumilli et al., 2020; Hellmer, 2004; Rignot et al., 2013) point to values at least double this, but there are two provisos. The first is that basal melt rates appear to vary significantly on annual and longer time-scales (Adusumilli et al., 2020) and the AABW sampled here is as much as a thousand years old (e.g., Jenkins, Doney, et al., 2023; Jenkins, Seltzer, et al., 2023). Thus, what is measured here reflects earlier, rather than current melt rates. Second, consideration of the mechanics of AABW formation and basal melting suggests that not all GMW will be incorporated into AABW formation (Adusumilli et al., 2020; Jacobs et al., 1992), and indeed, there is direct evidence of some portion that surfaces (Zheng et al., 2021) rather than being incorporated solely into bottom water. This means that our estimate of 450 ± 70 GT a^{-1} is a lower bound to the total rate of basal melting.

The broad deep-water ΔNe and Ne maxima (Jenkins, Doney, et al., 2023; Jenkins, Seltzer, et al., 2023) in the North Pacific, the former of which is visible in Figure 1a below 2,500 m depth and between 25 and 45°N, have a different signature and cause. The shape of the maximum is significant in that it appears centered around 35°N and ΔNe values begin to decrease slightly north of 45°N. The abyssal circulation in the North Pacific is characterized by a large-scale anticyclonic flow, first northward along the western boundary (Kato & Kawabe, 2009; Komaki & Kawabe, 2009), then eastward flow along the Aleutians (Owens & Warren, 2001) all the way to the Alaskan margin, followed by southward turn in the Gulf of Alaska (Hautala, 2018; Hautala & Hammond, 2020). Therefore, the maximum is a pool of the oldest, least recently ventilated waters. Table 2 summarizes the saturation anomaly differences between the AABW endmember characterized earlier and North Pacific Bottom Water (NPBW) component defined by the water below the 28.05 kg m^{-3} isoneutral horizon between 25° and 45°N.

Geothermal heating also affects the saturation anomalies (observe the positive trending black arrow in Figure 4). An analysis of CTD traces from bottom waters in the subarctic North Pacific by Joyce et al. (Joyce et al., 1986) reveals a net geothermal heating of approximately 0.05°C, which, using the solubility-temperature relationships (Jenkins, Lott, & Cahill 2019), leads to an increase of 0.05%, 0.13%, 0.16%, and 0.19% for ΔNe, ΔAr, ΔKr, and ΔXe respectively. The anomalies plotted in Figure 4 are corrected for this effect.

Unlike the PBW-NADW comparison, the observed NPBW-PBW changes in saturation anomalies are identical within errors for these four noble gases (after correcting for geothermal heating, see Figure 4) with a signature of a 2.8 ± 0.5 mbar paleo-barometric difference between the two regions (i.e., an average $0.28\% \pm 0.05\%$ PBW-to-NPBW increase in saturation anomalies for all four gases). Due to the long transit times from the sea surface where these water masses originated, and the effects of mixing along the path of the MOC, this must reflect an attenuated signal of a past sea level pressure decrease in the Antarctic Circumpolar Trough of 15 ± 6 mbar over the past two millennia, between the Roman Warm Period and the Little Ice Age (LIA) (Jenkins, Doney, et al., 2023; Jenkins, Seltzer, et al., 2023). It should be noted that the past change relative to the present Antarctic SLP is not constrained by these data (op. Cit.), but recent work points to a negative SLP anomaly for the LIA (Bertler et al., 2011; Rhodes et al., 2012; Simms et al., 2021). At least for the most recent millennia, evidence

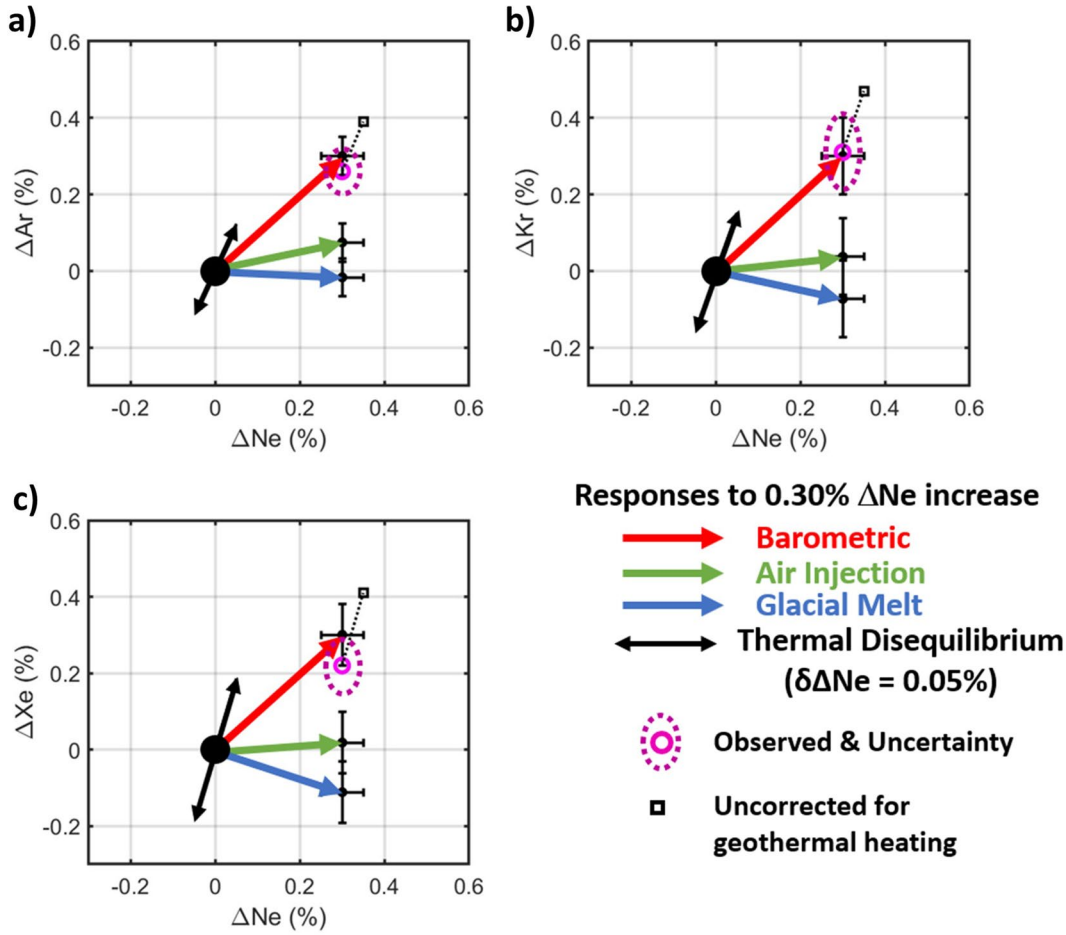

Figure 4. Schematic response in the heavy noble gas saturation anomalies (after correction for geothermal heating) to an increase of 0.30% in ΔNe by various processes (see text). The corrected changes between PBW and NPBW are shown as the magenta circles with the uncertainty expressed by the dotted ellipse (the original, uncorrected points are shown as black squares connected by the thin dotted black line).

for a long-term decrease in SLP is similarly supported by tree-ring records of the Southern Annular Mode index (Abram et al., 2014).

6. Deep Waters

Following the pathway of the MOC, we next discuss the deep waters in the North Pacific. Holzer et al. (Holzer et al., 2021) describe a circulation scheme where bottom waters enter the abyssal North Pacific, upwell, and turn southward at depths around or below 2,500 m. In other words, the portion of the water column between the low salinity intermediate waters and the arriving bottom waters is "maintained" by vertical advective-diffusive processes, which largely occur on the boundaries and over rough topography, and whose effects are redistributed by lateral mixing and advection (e.g., Kunze, 2017). Despite this complexity, vertical profiles of potential temperature and salinity in this region appear to closely follow an exponential relationship with depth, which led early workers to posit a one-dimensional advection-diffusion recipe to explain the vertical distributions of other properties (e.g., Munk, 1966). In this section, potential temperature and salinity profiles between 35 and 45°N fit the classic quasi-exponential curves with an average vertical scale height of 755 m, along with a linear Θ-S relationship (see Figure S3 in Supporting Information S1). Here, we invoke a "similarity model" based on the fact that the heavier noble gas concentrations also show this behavior (Figures 5a–5d), where the red line represents the exponential fit to the data. By "fit" we mean that we have used the same vertical scale height defined by the temperature and salinity curves and projected the curves through the interpolated top and bottom

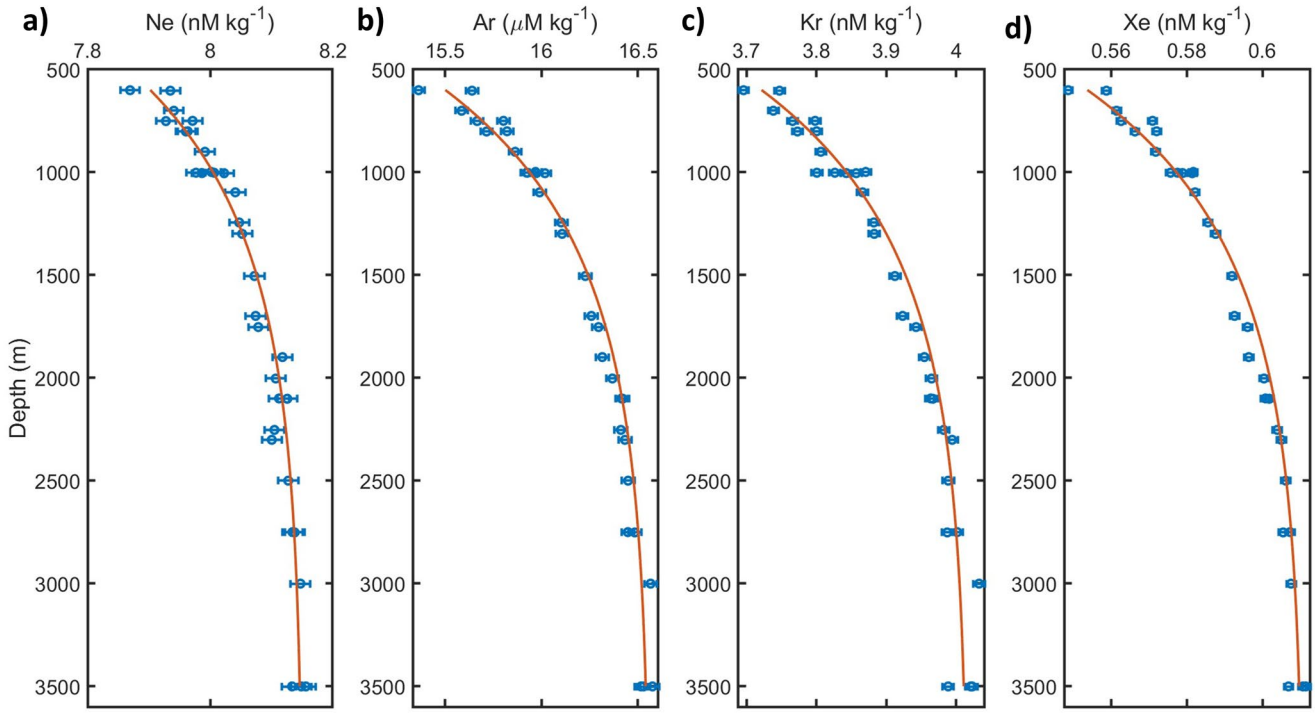

Figure 5. Depth profiles for the concentrations of (a) Ne, (b) Ar, (c) Kr, and (d) Xe for stations between 35 and 45°N. All concentrations are expressed in nM kg^{-1} except for Ar, which is in μM kg^{-1}. The red line is the projected values based on the mean top and bottom values using the exponential model with a scale height defined by potential temperature and salinity profiles (see Supporting Information S1).

end-member noble gas concentrations. Given their inert nature and lack of internal sources or sinks, the correspondence lends credence to the use of such a similarity model in this instance. One final aside is that despite the apparent vertical homogeneity of ΔNe in the North Pacific deep and bottom water evinced by Figure 1a, there is a very real vertical variation in the neon concentration profile while coincidentally the ΔNe remains approximately constant. The latter is solely a reflection of the coincidence between the upper and lower endmember saturation anomalies, not concentrations.

We recognize the caveats associated with applying such a simple model. In particular, the upwelling velocity likely decreases upward due to the upwelling waters turning southward at mid-depth. While this may affect quantitative flux calculations, the apparent consistency of stable conservative tracer profiles, especially all four noble gases, suggests that this simple model at least approximates the observed vertical tracer profiles within the limits of measurement uncertainties. Extending the model to helium and its isotopes (Figure 6) in effect is projecting what the vertical profile of those tracers should look like given their concentrations in the incoming bottom water flow in the absence of any in situ sources. Before doing this for ^{3}He, we need to consider the influence of tritiugenic ^{3}He. Although the deep waters are not directly influenced by the decay of bomb-tritium (see Figure 7a), which only penetrates to about 1,200 m at these latitudes, its presence and decay product (tritiugenic ^{3}He) will affect our choice of the upper end-member ^{3}He concentration for the similarity model fit. Comparing the tritium and δ^{3}He profiles (Figure 7b), we see that a very real tritiugenic excess begins to appear as one moves upward in the water column above 1,000 m depth. This feature has appeared in the past 50–60 years due to in situ decay of bomb tritium as it penetrates into the upper ocean. The issue is that during the time when the original deep-water gradients are established (centuries ago, before the bomb-tritium transient), the "original" end-member was lower and should only reflect natural tritiugenic ^{3}He addition.

To estimate and correct for the effect, we employ a lateral-mixing model successfully employed in the North Atlantic to explain the tritium-^{3}He relationship (Jenkins, 1980, 1988) driven by a sub-polar North Pacific surface tritium source function (Stark et al., 2004) extended to 2018 using recently compiled surface tritium data (Jenkins, Doney, et al., 2019). The "residence time" is obtained by matching the tritium concentration at the depth of the upper end-member (0.2 TU at 600 m in this case), and is used to predict the bomb tritiugenic ^{3}He excess

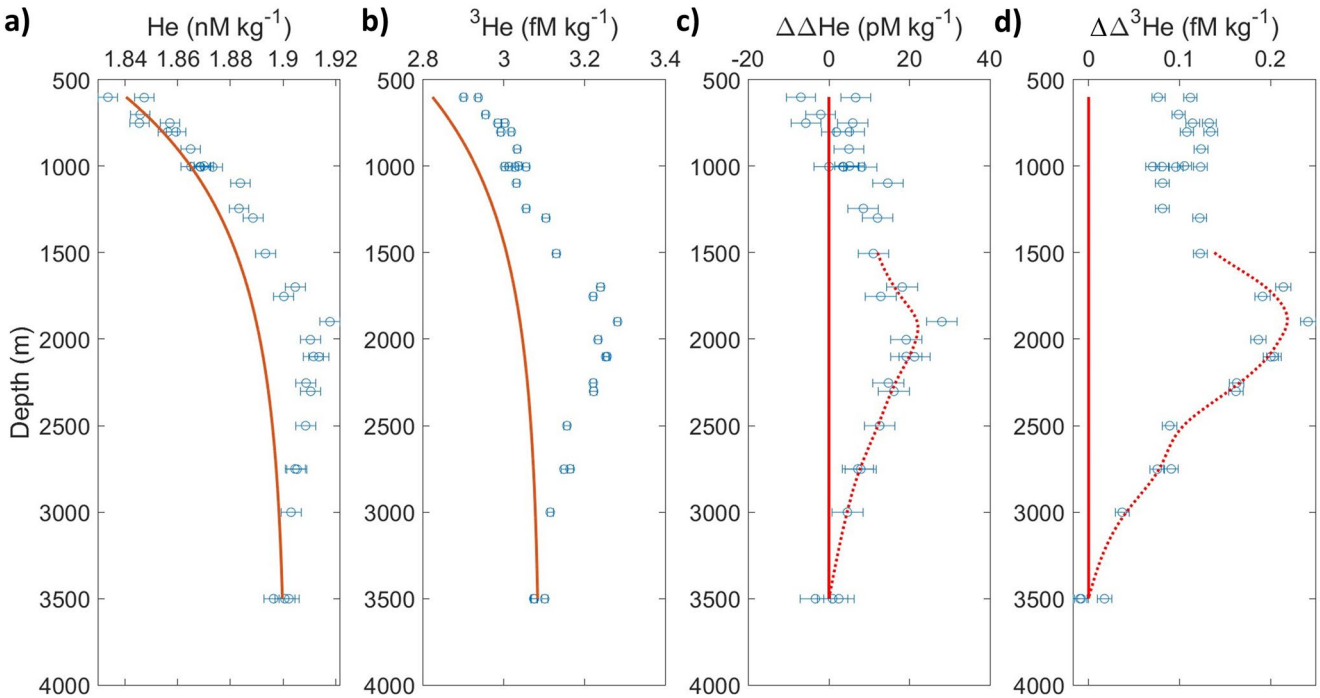

Figure 6. Depth profiles for the concentrations of (a) He (in nM kg^{-1}), (b) ^{3}He (in fM kg^{-1}), (c) the difference between He concentration and the similarity model curve (in pM kg^{-1}) and (d) the difference between ^{3}He concentration and the model curve (in fM kg^{-1}) for stations between 35 and 45°N. The solid red line is the projected values based on the mean top and bottom values using the model with a scale height defined by potential temperature and salinity profiles (see Supporting Information S1). Note that the ^{3}He end member has been altered to project to pre-anthropogenic (pre-bomb tritium decay) levels.

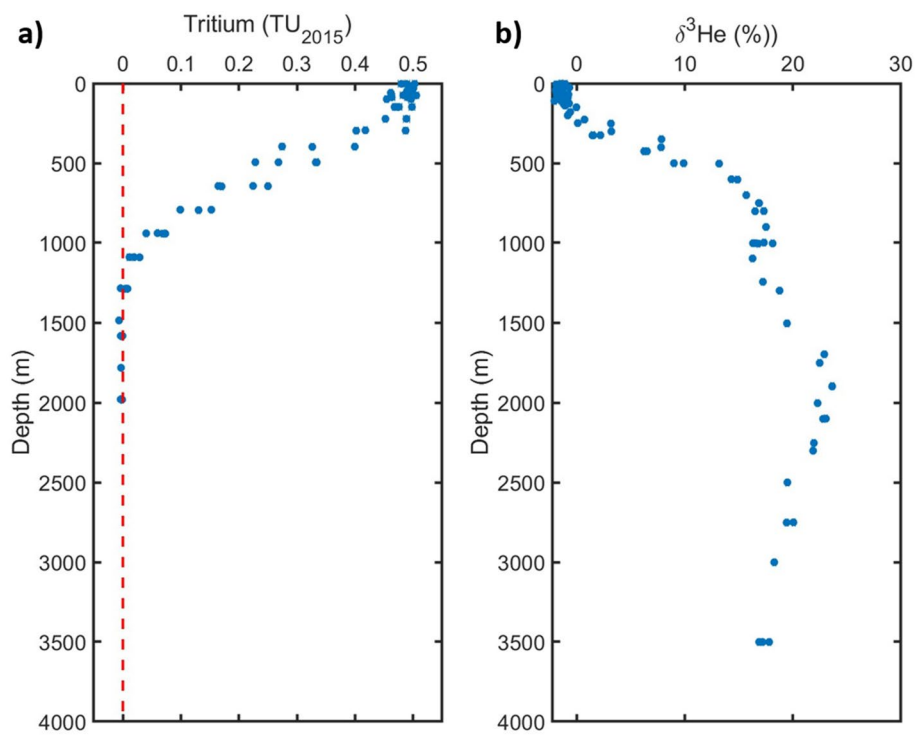

Figure 7. (a) Composite tritium profile (in TU$_{2015}$) measured in 2015 on this section between 35 and 45°N, and (b) composite δ^3He profile (in %) for stations between 35 and 45°N. Note that the data spread in the profiles is due to significant latitudinal gradients combined with the 10° spread of stations along the track.

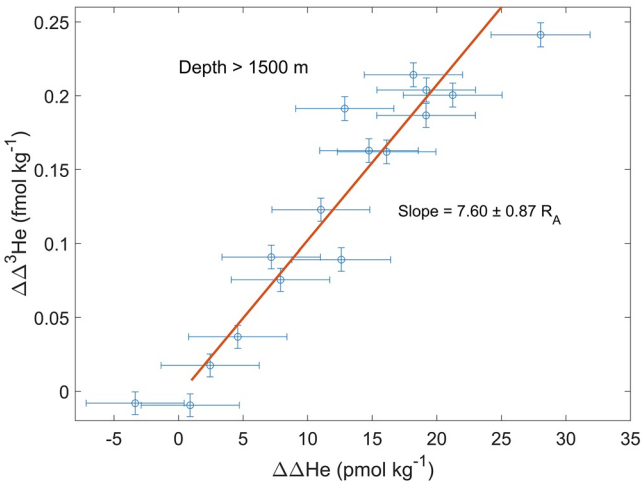

Figure 8. Weighted type II linear regression (red line) between $\Delta\Delta^3$He (in fM kg^{-1}) and $\Delta\Delta$He (in pmol kg^{-1}) for waters deeper than the penetration of tritium for stations between 35 and 45°N.

(0.145 fm kg^{-1}). Next, we use the same model, driven by pre-bomb tritium surface concentrations, and apply the same residence time to determine the expected natural tritiugenic ^{3}He excess (0.050 fm kg^{-1}), which we then subtract from the bomb tritiugenic ^{3}He excess. The result (0.095 fm kg^{-1}) is inferred to be the anthropogenic bomb-tritiugenic addition, and is subtracted from the observed interpolated 600 m ^{3}He concentration to formulate the upper end-member for the ^{3}He similarity model calculation in Figure 6b.

The mid-depth C(He) and C(^{3}He) profiles (Figures 6a and 6b) clearly deviate from the noble gas similarity model-predicted behavior (solid red lines), a consequence of the mid-depth injection of hydrothermal helium at other locations, perhaps south or east of this section, and the subsequent transport along horizontal gradients of those properties. It is this non-atmospheric helium that pulls the concentration profiles away from the noble gas-projected model profiles. The offset at the top end of the ^{3}He profile (where the red line is to the left of the data points) is a result of the correction described above. That is, the red line points to where we predict the pre-anthropogenic values would be. In the subsequent two plots (Figures 6c and 6d) we show this offset. Here we define $\Delta\Delta$He and $\Delta\Delta^3$He as the differences in concentration between the observed and model-interpolated values ($\Delta\Delta$He in pM kg^{-1} for Figure 6c and $\Delta\Delta^3$He in fM kg^{-1} for Figure 6d). The former should not be confused with the *saturation anomaly* ΔHe as defined by Equation 2. The $\Delta\Delta$He profile appears exactly as expected for mid-depth hydrothermal injection, where the $\Delta\Delta^3$He profile follows the same pattern at mid-depths but apparently diverges above 1,200–1,500 m depths due to tritium decay. Correlating the two deviations below 1,500 m depth (to avoid any possible tritiugenic ^{3}He contamination) we observe a demonstrably linear relationship with a ^{3}He/^{4}He slope of 7.60 ± 0.87 R$_A$ (Figure 8). It is important to note that this slope is the isotopic ratio of the helium being added to upwelling bottom waters, not the isotopic ratio of the resultant mixture. The ratio of the helium being added to upwelling AABW and PDW, although clearly larger than atmospheric, is slightly, but significantly lower than the known large deep-water hydrothermal sources of 8–10 R$_A$, which are largely injected into the deep waters at depths a few hundred meters above the mid-ocean ridges (Jenkins et al., 1978, 2018; Lupton, 1998a).

Extending this simple model to individual stations along this section (adjusting the upper depth limit of the model subrange according to the station's T-S relationship and using the upper end-member tritium concentrations to derive the tritiugenic contribution/offset to the top of the ^{3}He curve), we are able to estimate the excess helium and its isotope ratio for all but one station (where there were too few measurements in the critical depth range to obtain a robust ratio). Although the actual circulation likely violates the underlying simplifying assumptions of a one-dimensional model, we note that the model appears to do such a good job fitting the noble gas profiles that we are confident that it provides an adequate representation of the "background" helium distributions so that the excess helium ratio measurements are likely robust. We present the results in Figure 9 as function of latitude.

Within ±10° of the equator, the average excess helium isotopic ratio is 8.2 R$_A$ with a scatter of 0.4 R$_A$, (one standard deviation) which is, a value close to the canonical mid-ocean ridge hydrothermal values observed in the Pacific (Allegre et al., 1995; Jenkins et al., 1978; Kurz & Jenkins, 1981; Lupton, 1998a, 1998b). South of the 10°S, the average ratio is a little higher, 9.6 ± 0.3, somewhat greater than the 8.6 ± 0.3 obtained for the Southern East Pacific Rise (SEPR) Plume (Jenkins et al., 2018) but consistent with the higher values observed along the SEPR in glassy rinds of fresh basalts (Kurz et al., 2005). Meanwhile, the northern mid-latitudes (10–35°) are similar to the equatorial band at 8.1 ± 0.4 R$_A$, but with significantly higher scatter, likely due to larger statistical uncertainties. North of 40°N, the ratio trends significantly downward to the north, decreasing steadily to 2–4 R$_A$ near the Alaskan continental slope, an isotope ratio substantially lower than the known, documented submarine hydrothermal sources.

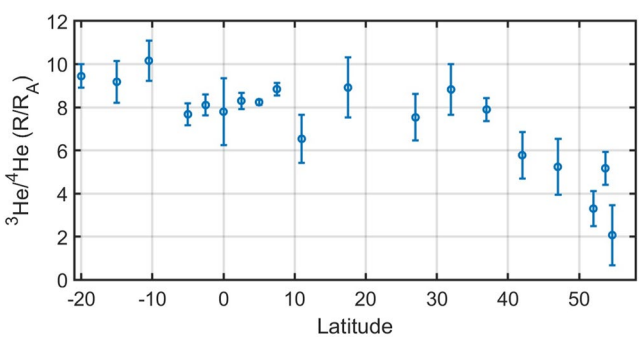

Figure 9. Similarity model calculated ^{3}He/^{4}He ratios (in R$_A$) of the deep water column added helium for stations in the section as a function of latitude.

It should be noted, however, that as one approaches the northern extreme of the section, the excess helium "signal" grows progressively smaller, particularly for the two northernmost stations (north of 54°N). In those cases, there are two potential mechanisms that might spuriously lower the apparent ^{3}He/^{4}He

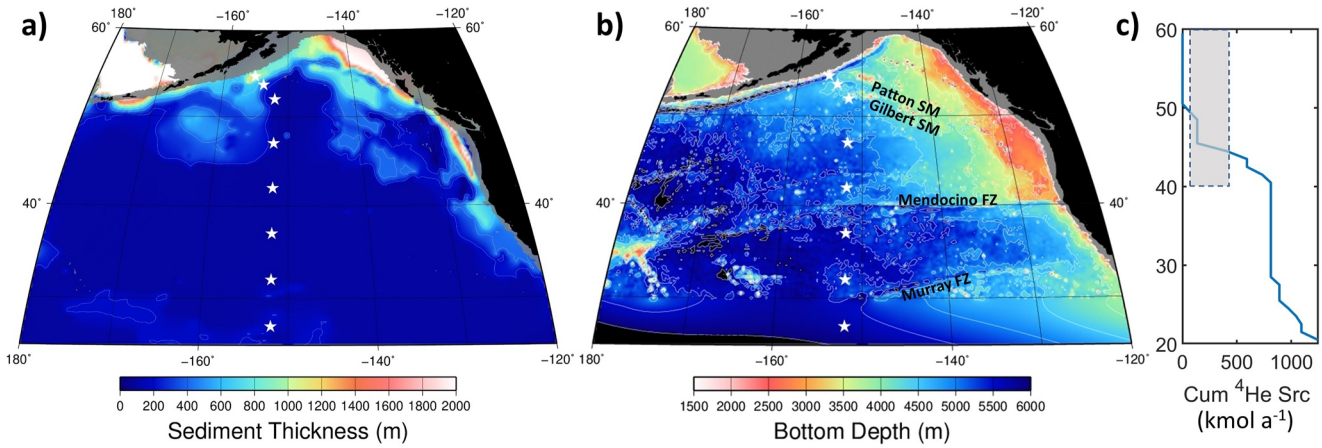

Figure 10. (a) Sediment thickness map for Northeast Pacific, taken from the GlobSed database (Straume et al., 2019). Deep station locations are shown as white stars. White areas are thicker than 2,000 m, land is black, and gray-masked areas are shallower than 1,500 m deep. (b) Bottom topography (from ETOPO-1). Depth greater than 6,000 m is black, as is land. (c) Cumulative (going from north to south) hydrothermal source of ^{4}He in kmol a^{-1} (blue line). The gray-shaded area is the range of sedimentary ^{4}He fluxes for the area north of 40°N.

ratio. The first is any unresolved positive-going paleo-barometric "signal" akin to the AABW—NPBW feature discussed earlier (Jenkins, Doney, et al., 2023; Jenkins, Seltzer, et al., 2023), which would manifest itself in an apparent positive ΔΔHe with a ΔΔ^{3}He increase that is close to atmospheric. However, such effect would also manifest itself in significant correlation coefficients between ΔΔHe and the other gases (ΔΔNe, ΔΔAr, ΔΔKr, and ΔΔXe) with a slope of +1 for each pair. The second confounding mechanism could arise from variable sampling-induced air injection. As the water sample is transferred from the Niskin rosette to the copper tube storage container on board the ship, there is a small possibility of trapped ambient air bubbles being forced into solution during acquisition. Although every effort is taken to ensure that this is avoided/minimized, the possibility remains. This would manifest itself in small positive ΔΔHe anomalies that would also be accompanied by progressively smaller correlations between ΔΔHe and the other noble gases. We use the term "progressively smaller" because the relative solubilities of those gases mean that their relative magnitudes of the perturbaions are approximately 0.8, 0.25, 0.15, and 0.08 times the size of ΔΔHe for ΔΔNe, ΔΔAr, ΔΔKr, and ΔΔXe respectively. Given experimental errors, in practice, this second effect would result in only a significant correlation between ΔΔHe and ΔΔNe. Examining the inter-anomaly correlation coefficients for the northern stations, we find that there is no significant correlation between ΔΔHe and the heavy (ΔΔAr—ΔΔXe) gases, thus eliminating the paleo-barometric effect. We find only a marginal correlation with ΔΔNe for the two northern-most stations ($p \sim 0.1$ and $p \sim 0.2$), so it seems doubtful that sampling artifacts play a role in lowering the apparent ^{3}He/^{4}He ratio. Even if those two stations were excluded, the northward decline in ^{3}He/^{4}He ratio is still robust.

7. Sources of Low ^{3}He/^{4}He Helium

Aside from the atmosphere, there are a number of possible sources of helium with ^{3}He/^{4}He ratios lower than the canonical hydrothermal 8 R_A observed throughout the bulk of the deep Pacific. All derive ultimately from the decay products of long-lived U and Th isotopes that in a variety of lithological environments produce helium isotope ratios ranging from 0.01–0.1 R_A (Andrews, 1985; Morrison & Pine, 1955). One possible origin is the loss of radiogenic helium from deep-sea sediments, which are more abundant in the Gulf of Alaska (see Figure 10a). Pore-water measurements in deep-sea sediments at locations in the east equatorial and northeast Pacific encompass a range of radiogenic helium fluxes spanning 0.6–8.4 × 10^{-8} mol m^{-2} a^{-1} (Barnes & Bieri, 1976; Sayles & Jenkins, 1982). The possibility of significant addition of sedimentary radiogenic helium is buttressed by the observation of significant geothermal heating in the abyssal sub-Arctic Pacific (Joyce et al., 1986) despite the absence of active seafloor spreading this far north. The northward decrease in deep-water excess ^{3}He/^{4}He appears to begin at ~40°N, the approximate latitude of the Mendocino Fracture Zone (see Figure 10b), which marks the boundary between northern and southern deep-water circulations in the northeast Pacific (see Hautala, 2018, also see Reid, 1997; plus see discussion in Supporting Information S1). At the longitude of this section north of 30°N, the deep water flow is predominately southward or south-southeastward, appearing to originate north of the Patton

and Gilbert Seamounts (see Figure 5 of Hautala, 2018 for NS18, which corresponds to ~2,500 m depth), presumably originating ultimately from the northern boundary current and upwelling NPBW. There, sediment thicknesses increase significantly compared to the lower latitudes, exceeding 2 km on the southern continental slope of Alaska. Indeed, sediment thicknesses are greater throughout the Gulf of Alaska (see Figure 10a, constructed from GlobSed (Straume et al., 2019)). Using GlobSed, we find an area of 4.9×10^6 km^2 (4.9×10^{12} m^2) at depths exceeding 1,500 m that are covered by sediments thicker than 100 m. Using the broad range of ^{4}He fluxes above, we estimate a possible sedimentary flux of 30–420 kmol a^{-1} entering the basin north of 40°N and south of the Alaskan continental slope. It is enlightening to compare this range of fluxes to the estimated hydrothermal input of ^{4}He from current models. Scaling the global model source function used in the CMIP6 Ocean Model Intercomparison Project (Orr et al., 2017) to match recent best estimates of global hydrothermal ^{3}He fluxes (Bianchi et al., 2010; DeVries & Holzer, 2019; Schlitzer, 2016), we calculate the cumulative hydrothermal ^{4}He source between 180°W and the North American continent (going from north to south, following the bulk of bottom water flow in this basin) in Figure 10c. Note that there are no documented deep-water hydrothermal sources north of 50°N in the model source, and to our knowledge, none of significance has been identified. Overlaid on this curve is our estimated sedimentary flux range (light gray box) for comparison. Although the range is broad, it is conceivable that it may be significant in this area. In other words, given that the bulk of the hydrothermal sources are far to the south, and the deep northern portion of the Gulf of Alaska is a relative stagnation point in the global MOC, it is feasible that the sedimentary flux may partially account for the northward decline in added ^{3}He/^{4}He ratio.

The modeled absence of significant deep-water hydrothermal helium sources north of ~50°N is due to the fact that the East Pacific Rise spreading axis intersects the North American continent at about 28°N in the Guaymas Basin, and the Juan de Fuca Ridge (JdFR) terminates just north of Vancouver Island at about this latitude, and sea-floor spreading gives way to convergent subduction zone tectonics in the North. This suggests another, and perhaps more likely source, that is, venting from seeps in the large sedimentary accretionary wedge or prism along the Alaskan and North American continental slopes. These relatively ancient sediments will have large amounts of accumulated radiogenic helium and other gases that can leak back into the ocean. The Alaskan convergent margin shows imbricate structures punctuated by faults (Moore & Vrolijk, 1992), which vastly enhance fluid transfer and expulsion of gases and creation of vent fields (von Huene et al., 1998). This is further evidenced by developed biological communities (Suess et al., 1998) along the Alaskan slope. Such activity is also seen along the North Pacific margin of North America (Campbell et al., 2002). Although we are unaware of any helium isotope measurements of cold-seep gases along the Alaskan prism, observation of relatively "low" helium isotope ratios (0.1–2.4 R_A) in the Cascadia continental margin, just south of where the JdFR intersects the continent, shows a mixture of "mantle" and radiogenic helium (Baumberger et al., 2018). Quantifying the overall contribution of these seeps to the water column budgets is impossible at this time, but bears consideration in future.

In summary, we can attribute the observed decline in the isotope ratio of helium added to the abyssal water column north of 40°N in the Pacific to one or both of the two possible sources: the diffusion of radiogenic helium from abyssal marine sediments in the Gulf of Alaska or leakage of radiogenic helium from accretionary prism sediments on the continental margins of North America and Alaska. Note, however, the net reduction in the seawater ^{3}He/^{4}He ratio due to this influx may be small. That is, we have determined the isotopic ratio of the *added* helium whereas the actually observed isotope ratio of the dissolved helium in a water parcel reflects the integrated ratio of all helium added to that parcel since it was last equilibrated with the atmosphere. To correctly establish the water parcel's helium isotope ratio, we need to develop a means of computing the actual excess ^{3}He/^{4}He present in the next section.

8. Excess Helium Isotopes

We reported a method for computing excess helium isotopes in seawater (Jenkins et al., 2018) that expressed the excess (non-atmospheric) helium isotopes as

$$C_{XS}(^4\mathrm{He}) = C_M(^4\mathrm{He}) - C_S(^4\mathrm{He}) - C_A(^4\mathrm{He})$$
$$C_{XS}(^3\mathrm{He}) = C_M(^3\mathrm{He}) - C_S(^3\mathrm{He}) - C_A(^3\mathrm{He}) \quad (3)$$

Where the subscript M refers to the measured concentrations, S refers to the solubility concentrations (Jenkins, Lott, & Cahill 2019), and A refers to the atmospherically injected gases (excess atmospheric component), created by bubble dissolution at the sea surface. While adequate for predicting the abundance of non-atmospheric ^{3}He in

Pacific Deep Waters, this formulation neglected a potentially important source that could impact our estimates of non-atmospheric ^{4}He. As discussed earlier in the paper, a significant component of Antarctic Bottom Water, the progenitor of Pacific bottom and deep water, involves glacial melt water (GMW) that is produced by basal melting of Antarctic ice shelves. Dissolved noble gas saturation anomalies in GMW are profoundly affected by both the dissolution, under high hydrostatic pressure, of trapped glacial air (Gow & Williamson, 1975; Hohmann et al., 2002) as well as thermohaline alterations due to the latent heat of fusion ("Gade" effects) (Gade, 1993; Loose & Jenkins, 2014). Independent estimates of the Antarctic GMW production range from ~500–1,300 Gt a^{-1} (Hellmer, 2004, this work; Rignot et al., 2013) and observations of in situ noble gas saturation anomalies point to GMW components as high as 0.3%–0.35% (Loose et al., 2016; Nicholson et al., 2016) in Circumpolar Deep Water. We therefore include this term as

$$\begin{aligned} C_{XS}(^4\mathrm{He}) &= C_M(^4\mathrm{He}) - C_S(^4\mathrm{He}) - C_{\mathrm{GMW}}(^4\mathrm{He}) - C_A(^4\mathrm{He}) \\ C_{XS}(^3\mathrm{He}) &= C_M(^3\mathrm{He}) - C_S(^3\mathrm{He}) - C_{\mathrm{GMW}}(^3\mathrm{He}) - C_A(^3\mathrm{He}) \end{aligned}, \tag{4}$$

where the reason for the ordering of the terms becomes evident below.

The first terms on the right-hand side of Equation 4 are given by

$$\begin{aligned} C_M(^4\mathrm{He}) &= C_M(\mathrm{He}) \\ C_M(^3\mathrm{He}) &= 1.384 \times 10^{-6}(1 + \delta(^3\mathrm{He})/100) \times C_M(\mathrm{He}) \end{aligned}. \tag{5}$$

Note that since atmospheric helium is ~99.9999% ^{4}He, we have $C_M(^4\mathrm{He}) = C_M(\mathrm{He})$. The second equation in Equation 5 uses the observed helium isotope ratio anomaly and the atmospheric ^{3}He/^{4}He ratio (Clarke et al., 1976) to compute the measured concentration of ^{3}He.

The second terms in Equation 4 are derived from the solubility as a function of potential temperature and salinity of each sample, combined with the helium isotope solubility fractionation factor α_S which is a function of temperature and salinity (Benson & Krause, Jr., 1980):

$$\begin{aligned} C_S(^4\mathrm{He}) &= C_S^0(\mathrm{He}) \times \left(1 + \frac{\Delta\Delta\mathrm{He}}{100} + \Delta P\right) \\ C_S(^3\mathrm{He}) &= \alpha_S \times 1.384 \times 10^{-6} \times C_S(^4\mathrm{He}) \end{aligned} \tag{6}$$

C_S^0 is the solubility equilibrium concentration, which is a function of potential temperature and salinity, measured at precisely one atm pressure (Jenkins et al., 2019a), and where $\Delta\Delta$He is our estimate of the saturation expectation inflation due to diapycnal mixing (estimated from ΔAr, ΔKr, and ΔXe as described by Jenkins et al. (2018)) which must be added back in (see Supporting Information S1). In addition, ΔP is a fractional pressure adjustment to account for the fact that sea level pressure is generally less than precisely one atm during water mass formation. In essence, this term serves to repartition the helium isotopic and atmospheric excess Ne corrections between the "solubility" and "atmospheric/injected" components. The overall effect is modest (see later discussion), so the "precision" of the correction need not be great. Using NCEP reanalysis data over a 60-year period (1960–2020) for winter-time sea level pressure in four representative water mass formation regions (two each in the Weddell and Ross Seas), we find SLP averages of 0.973 and 0.972 atm for Weddell and Ross Seas respectively. The Southern Ocean SLP is characteristically low, being controlled by the strength of the Antarctic circumpolar trough, a persistent low pressure belt that surrounds the Antarctic continent (e.g., Gong & Wang, 1999; Gordon et al., 2007; Meredith & Hogg, 2006; Schlosser et al., 2011). Inasmuch as the bulk of Pacific bottom and deep waters originate from these regions, we use this estimate of the average SLP anomaly for the Ross and Weddell Seas and assume an uncertainty (see Supporting Information S1) to obtain

$$\Delta P_0 = -0.028 \pm 0.005 \tag{7}$$

where we use the subscript 0 to designate that it is a constant in our formulation.

In addition, we account for a long-term secular change in sea level pressure over time, as reported earlier (Jenkins, Doney, et al., 2023; Jenkins, Seltzer, et al., 2023). Here we introduce an arbitrary spatial function (of latitude and depth) that approximates the observed distribution of ΔNe anomaly and whose spatial average value (between 25 and 45°N and below 3,500 m depth) is 0.0028, according to

$$\Delta P = \Delta P_0 + 0.0038 \sin\left(\pi \frac{\varphi - 20}{40}\right)^{0.125} \times \sin\left(\pi \frac{d - 2000}{3500}\right)^{0.125}$$
$$15 < \varphi < 55 \quad \text{and} \quad 2000 < d < 5500\,\text{m} \tag{8}$$
$$\Delta P = \Delta P_0 \quad \text{elsewhere}$$

An important constraint on the magnitude of the third terms in Equation 4 lies in the consideration of the mean saturation anomaly of neon. As discussed earlier, the inflowing bottom water for this section has a mean $\Delta\text{Ne} = 1.66\% \pm 0.05\%$, whereas the average North Atlantic Deep Water, based on observations in the deep subtropical North Atlantic (Jenkins et al., 2015) and in the Labrador Sea (Hamme et al., 2019), has a mean $\Delta\text{Ne} = 0.90\% \pm 0.05\%$. The difference is attributable to the addition of GMW since the aggregate amount required (given the production rates of AABW and NADW) is consistent with known rates of basal melting around Antarctica, and with estimates of GMW fractions in the Southern Ocean (Jullion et al., 2014; Loose et al., 2016). Thus, we attribute a net Ne increase of 6.05×10^{-11} mol kg^{-1}, which using the GMW He/Ne ratio of 0.2880 gives a GMW helium contribution of 17.4 pmol kg^{-1}. Given this is atmospheric helium, we arrive at

$$C_{\text{GMW}}(^4\text{He}) = 17.4\,\text{pmol kg}^{-1}$$
$$C_{\text{GMW}}(^3\text{He}) = 0.0241\,\text{fmol kg}^{-1} \tag{9}$$

Finally, for the fourth set of terms, we used a heuristic relationship to predict the atmospherically derived ΔHe produced by the combination of air bubble injection (e.g., Jenkins, 1988), thermal disequilibrium (Hamme & Severinghaus, 2007), and differential gas exchange (Stanley, Jenkins, et al., 2009). Given the similarities in colligative properties between He and Ne, we use ΔNe as a predictor of the atmospheric (air injected) ΔHe. As described in Supporting Information S1, we combined a global database of deep-water observations and deep convection models at two sites using a range of gas exchange formulations to predict an average excess atmospheric helium/neon slope of 0.230 ± 0.004. The fact that this value is significantly lower than the atmospheric He/Ne abundance ratio of 0.288 is a reflection of the intertwined effects of thermal disequilibrium (Hamme & Severinghaus, 2007) and partial versus complete bubble injection processes (Jenkins, 1988; Liang et al., 2013; Stanley, Jenkins, et al., 2009) during water mass formation. The factor used is slightly higher than, but within errors of the 0.22 ± 0.01 used earlier (Jenkins et al., 2018), but this has a negligible effect on the $C_{XS}(^3\text{He})$ and a very small effect on the $C_{XS}(^4\text{He})$ calculations. Thus, we have

$$C_A(^4\text{He}) = (0.230 \pm 0.004) \times C_A(\text{Ne})$$
$$C_A(\text{Ne}) = \frac{\Delta\text{Ne} - \Delta\Delta\text{Ne} - \Delta P}{100} C_S^0(\text{Ne}) - C_{\text{GMW}}(\text{Ne}) \tag{10}$$
$$= \frac{\Delta\text{Ne} - \Delta\Delta\text{Ne} - \Delta P}{100} C_S^0(\text{Ne}) - 60.4\text{pmol kg}^{-1}$$

where we have likewise corrected for a glacial meltwater contribution for Ne to the apparent supersaturation. Note that the ΔP term appears in this case to *increase* the effective air injection neon component because the original definition of ΔNe is relative to saturation at precisely one atm (Equation 2). This leads to an estimate of the atmospheric helium excess:

$$C_A(^4\text{He}) = (0.230 \pm 0.003) \times \left[\frac{\Delta\text{Ne} - \Delta\Delta\text{Ne} - \Delta P}{100} C_S^0(\text{Ne}) - 60.4\text{pmol kg}^{-1}\right]$$
$$C_A(^3\text{He}) = 1.384 \times 10^{-6} \times C_A(^4\text{He}) \tag{11}$$

where again we use superscript 0 for the Ne solubility to emphasize that it is the empirically determined solubility of Ne at the potential temperature and salinity of the sample at precisely one atm, that we have corrected ΔNe for the mixing-induced increase (ΔΔNe) using observations of ΔAr, ΔKr, and ΔXe as described earlier (Jenkins et al., 2018), that the 0.76% is subtracted to correct for the GMW contribution to the Ne (the corresponding GMW He addition is explicitly accounted for), and finally that the ΔP term is introduced to account for the barometric anomaly described earlier. Note that the two correction factors (ΔΔHe and ΔΔNe) act in a somewhat compensatory fashion. That is, ΔΔHe serves to inflate the apparent value of C_S while ΔΔNe reduces the contribution of C_A in Equation 4. We arrive at

$$C_{XS}(^4\mathrm{He}) = C_M(^4\mathrm{He}) - C_S^0(^4\mathrm{He}) \times \left(1 + \frac{\Delta\Delta\mathrm{He}}{100} + \Delta P\right) - 17.4\mathrm{pmol\,kg^{-1}}$$
$$-(0.230 \pm 0.004) \times \left[\frac{\Delta\mathrm{Ne} - \Delta\Delta\mathrm{Ne} - \Delta P}{100} C_S^0(\mathrm{Ne}) - 60.4\mathrm{pmol\,kg^{-1}}\right]$$
$$C_{XS}(^3\mathrm{He}) = C_M(^3\mathrm{He}) - \alpha_S \times 1.384 \times 10^{-6} \times C_S^0(^4\mathrm{He}) \times \left(1 + \frac{\Delta\Delta\mathrm{He}}{100} + \Delta P\right) - 0.0241\mathrm{fmol\,kg^{-1}} \quad (12)$$
$$-1.384 \times 10^{-6} \times (0.230 \pm 0.004) \times \left[\frac{\Delta\mathrm{Ne} - \Delta\Delta\mathrm{Ne} - \Delta P}{100} C_S^0(\mathrm{Ne}) - 60.4\mathrm{pmol\,kg^{-1}}\right]$$

Thus, we compute the excess helium isotopes and their ratio for all depths greater than 1,000 m. The values are reported as a spreadsheet in Table S3, and presented in Figures 11a–11c. The propagation of errors in the various terms leads to an error estimate of 0.006 fmol kg^{-1} for $^3He_{XS}$ (~tenth of the contour interval in Figure 11a) and 4 pmol kg^{-1} for $^4He_{XS}$ (~half of the contour interval in Figure 11b).

For the three major deep-water features described earlier, the abundances of the two isotopes mirror each other almost exactly, lending confidence to the validity of the calculations. The northernmost maximum appears clearly separated from the other two deep features in neutral density anomaly space (upper panels). The intermediate depth feature appears more broadly distributed for $^3He_{XS}$ than for $^4He_{XS}$ because the isotope ratio of the vent helium is close to 27 R_A, that is, about triple that of the deep-water features (8–10 R_A), because it is sourced by a more primitive mantle feature (the Hawaiian Plume) while the others originate from mid-ocean ridge spreading centers which have a depleted mantle signature (Kurz & Jenkins, 2019; Kurz et al., 1982).

The propagation of errors yields random uncertainty in the excess helium isotopic ratio (Figure 11c) of order 0.4 R_A throughout most of the deep water, and is dominated by the relative uncertainty in $^4He_{XS}$. The appearance of single point anomalies ("blobs") in the deeper water (>2,500 m) is consistent with random errors of this magnitude. However, uncertainty in the water mass formation pressure correction leads to larger systematic uncertainty of 0.1 R_A. The uncertainty in the ratio becomes larger in the intermediate and shallower depths as the magnitude of $^4He_{XS}$ becomes progressively smaller (excluding the environs of Kama'ehuakanaloa Seamount). In the shallowest waters, the actual uncertainty is even greater because the introduction of tritiugenic ^3He from the decay of bomb tritium in and above intermediate waters drives the ratio systematically up. In that instance, we utilize the observations in a different manner, which is the topic of the accompanying paper (Jenkins, Doney, et al., 2023; Jenkins, Seltzer, et al., 2023).

Ten degree binned average values as a function of latitude are shown in Figure 11d for the deep-water ($27.8 < \gamma^N < 28.05$ kg m^{-3}) in the upper panel, and for bottom water ($\gamma^N > 28.05$ kg m^{-3}) in the lower panel, where the error bars are the standard error of the mean for each bin. The deep-water binned ratios (upper panel) increase monotonically southward because the deep water accumulates hydrothermal helium as it progresses southward on its way to the Southern Ocean. This is expected as mid-ocean ridge hydrothermal systems contribute helium with an isotopic ratio (>8 R_A) greater than that of the upwelling bottom water (~7 R_A) that feeds the deep-water flow. Using a simpler heuristic, Well et al. (Well et al., 2001) found lower mid-depth ratios along 135°W, having ~7.4 R_A (vs. 7.9 R_A) at 10°S, the latitude of the SEPR plume, ~6.8 R_A (vs. 7.5 R_A) at 10°N, the latitude of the NEPR plume, and ~6.8 R_A (vs. 7.3 R_A) at 35°N, the latitude of the Juan de Fuca plume. We believe that this difference is due to the manner in which the ratios are calculated, rather than the zonal separation of the sections.

Below, there is clear evidence of latitudinal variations that are consistent with the bottom water circulation discussed earlier and in Supporting Information S1 (also Figure S2 in Supporting Information S1). Note that the youngest bottom water enters this section from the south, but a more circuitous branch also enters via boundary flow from the west at the extreme northern end of the section and flows southward toward 30°N, picking up radiogenic helium either from abyssal sediments or the cold seeps along the Alaskan and North American sedimentary wedge/subduction zone. Further to the south, this water joins with water entering from the south in a westward flow at about 10–15°N, where we see the lowest accumulated $XS^3He/^4He$ ratio of ~6.3 R_A compared to ~6.8 R_A for the southern component. All along this tortuous route, bottom waters continue to upwell and feed the southward returning deep-water, whose $XS^3He/^4He$ ratio progressively increases to ~8 R_A by 20°S where it exits the section. Further downstream, this deep water must join the Circumpolar Current, which, in turn, must further up-well and seed the formation of AABW.

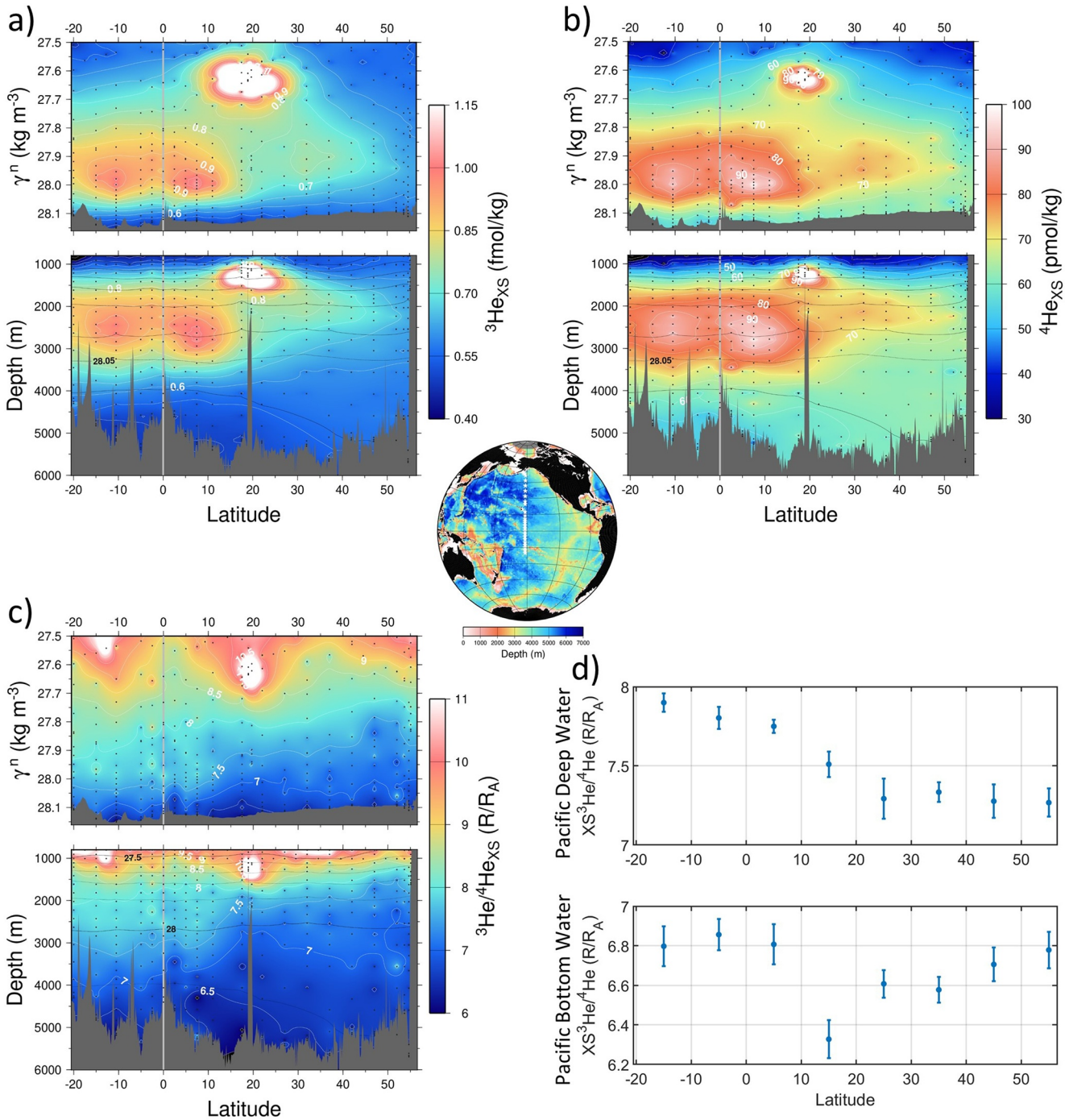

Figure 11. Sections of calculated (a) excess ^{3}He (in fmol kg^{-1}), (b) excess ^{4}He (in pmol kg^{-1}), (c) excess helium isotope ratio (in R/R$_A$), and (d) 10° averaged Pacific Deep Water (upper panel) and Bottom Water (lower panel) excess ^{3}He/^{4}He ratio (R/R$_A$).

9. Concluding Remarks

Characterizing the global distribution of the non-atmospheric helium inputs will require a broader coverage of high-quality noble gas and helium isotope measurements to fully account for all possible inputs. Recent refinements in sampling and analysis methodology clearly indicate that the distribution of neon in particular, but also the heavier noble gases is systematic and consistent with what is known about air-sea and sea-ice interactions. Our personal experience, based on many thousands of samples and many dozens of cruises, is that traditional sampling methods involving

clamped, 9.5 mm O.D. copper tubing, as well as the stainless steel valved cylinders, are prone to spurious bubble trapping during sample acquisition that confuses the true picture of atmospheric helium components. Thus, we recommend adopting the methodology developed by Lupton and co-workers (Young & Lupton, 1983). In any case, when interpreting historical data, it is prudent to be aware of the detailed sampling method used to acquire these data. This may not always be available, but recent compilations (e.g., Jenkins, Doney, et al., 2019) do provide this information.

This study shows how precise measurements of noble gases and helium isotopes on ocean sections can provide valuable information on geochemical, oceanographic, and earth system processes. The fact that the noble gases are inert yet span a wide range in physical characteristics make them powerful probes of interfacial exchanges. Such processes range from Antarctic glacial melting, past changes in sea-level pressure, bottom water formation and circulation, through radiogenic helium input and hydrothermal fluxes in the deep ocean. Combining high-quality noble gas tracer data with powerful inverse methods (e.g., Gebbie & Huybers, 2010, 2012) may prove a fruitful future endeavor for untangling and revealing climatically important processes such as past changes in glacial melt water rates, air-sea exchange, and sea level pressure.

Data Availability Statement

The GP15 data have been archived at the U.S. BCO-DMO (Biological and Chemical Oceanography Data Management Office) (Jenkins et al., 2022a, 2022b). The Ne data (Jenkins & German, 2021a, 2021b) are available under two DOI references: https://doi.org/10.26008/1912/bco-dmo.862182.1 and https://doi.org/10.26008/1912/bco-dmo.862220.1, and the Ar, Kr, and Xe data under https://doi.org/10.26008/1912/bco-dmo.877873.1 and https://doi.org/10.26008/1912/bco-dmo.877899.1. The hydrographic (pressure, temperature, and salinity) data are available with DOI references https://doi.org/10.26008/1912/bco-dmo.777951.6 and https://doi.org/10.26008/1912/bco-dmo.824867.5 respectively. The GO-SHIP tritium, helium isotope, and noble gas data are archived at the CLIVAR and Carbon Hydrographic Data Office (CCHDO) under DOI reference https://doi.org/10.7942/C2RP43.

Acknowledgments
This research was funded by U.S. National Science Foundation Grants OCE-1756138 (GEOTRACES 2018 section) and OCE-1536384 (GOSHIP 2015 section). We are grateful to Zoe Sandwith for shipboard sampling, and as always to the ODF water catchers, the ships' marine crews, and the cruise chief scientists. We thank Arnold Gordon, Bob Anderson, and Mark Kurz for their helpful suggestions and probing questions. We also thank the reviewers of this paper for constructive and helpful criticisms that significantly improved the final product.

References

Abram, N. J., Mulvaney, R., Vimeux, F., Phipps, S. J., Turner, J., & England, M. H. (2014). Evolution of the Southern Annular Mode during the past millennium. *Nature Climate Change*, *4*(7), 564–569. https://doi.org/10.1038/nclimate2235

Adusumilli, S., Fricker, H. A., Medley, B., Padman, L., & Siegfried, M. R. (2020). Interannual variations in meltwater input to the Southern Ocean from Antarctic ice shelves. *Nature Geoscience*, *13*(9), 616–+. https://doi.org/10.1038/s41561-020-0616-z

Allegre, C. J., Moreira, M., & Staudacher, T. (1995). ^{4}He/^{3}He dispersion and mantle convection. *Geophysical Research Letters*, *22*(17), 2325–2328. https://doi.org/10.1029/95gl02307

Andrews, J. N. (1985). The isotopic composition of radiogenic helium and its use to study groundwater movement in confined aquifers. *Chemical Geology*, *49*(1–3), 339–351. https://doi.org/10.1016/0009-2541(85)90166-4

Barnes, R. O., & Bieri, R. H. (1976). Helium flux through marine sediments of the northeast Pacific Ocean. *Earth and Planetary Science Letters*, *28*(3), 331–336. https://doi.org/10.1016/0012-821x(76)90194-1

Baumberger, T., Embley, R. W., Merle, S. G., Lilley, M. D., Raineault, N. A., & Lupton, J. E. (2018). Mantle-derived helium and multiple methane sources in gas bubbles of cold seeps along the Cascadia continental margin. *Geochemistry, Geophysics, Geosystems*, *19*(11), 4476–4486. https://doi.org/10.1029/2018gc007859

Beaird, N., Straneo, F., & Jenkins, W. J. (2015). Spreading of Greenland meltwaters in the ocean revealed by noble gases. *Geophysical Research Letters*, *42*(18), 7705–7713. https://doi.org/10.1002/2015gl065003

Benson, B. B., & Krause, D., Jr. (1980). Isotopic fractionation of helium during solution: A probe for the liquid state. *Journal of Solution Chemistry*, *9*(12), 895–909. https://doi.org/10.1007/bf00646402

Bertler, N. A. N., Mayewski, P. A., & Carter, L. (2011). Cold conditions in Antarctica during the Little Ice Age—Implications for abrupt climate change mechanisms. *Earth and Planetary Science Letters*, *308*(1–2), 41–51. https://doi.org/10.1016/j.epsl.2011.05.021

Bianchi, D., Sarmiento, J. L., Gnanadesikan, A., Key, R. M., Schlosser, P., & Newton, R. (2010). Low helium flux from the mantle inferred from simulations of oceanic helium isotope data. *Earth and Planetary Science Letters*, *297*(3–4), 379–386. https://doi.org/10.1016/j.epsl.2010.06.037

Biddle, L. C., Loose, B., & Heywood, K. J. (2019). Upper ocean distribution of glacial meltwater in the Amundsen Sea, Antarctica. *Journal of Geophysical Research: Oceans*, *124*(10), 6854–6870. https://doi.org/10.1029/2019jc015133

Bryden, H. L., Roemmich, D., & Church, J. (1991). Ocean heat transport across 24°N in the Pacific. *Deep-Sea Research*, *38*(3), 297–324. https://doi.org/10.1016/0198-0149(91)90070-v

Butterfield, D. A., Massoth, G. J., McDuff, R. E., Lupton, J. E., & Lilley, M. D. (1990). Geochemistry of hydrothermal fluids form axial seamount hydrothermal emissions study vent field, Juan de Fuca Ridge: Subseafloor boiling and subsequent fluid-rock interaction. *Journal of Geophysical Research*, *95*(B8), 12895–12921. https://doi.org/10.1029/jb095ib08p12895

Campbell, K. A., Farmer, J. D., & Des Marais, D. (2002). Ancient hydrocarbon seeps from the Mesozoic convergent margin of California: Carbonate geochemistry, fluids and palaeoenvironments. *Geofluids*, *2*(2), 63–94. https://doi.org/10.1046/j.1468-8123.2002.00022.x

Clarke, W. B., Beg, M. A., & Craig, H. (1969). Excess ^{3}He in the sea: Evidence for terrestrial primordial helium. *Earth and Planetary Science Letters*, *6*(3), 213–220. https://doi.org/10.1016/0012-821x(69)90093-4

Clarke, W. B., Jenkins, W. J., & Top, Z. (1976). Determination of tritium by spectrometric measurement of ^{3}He. *The International Journal of Applied Radiation and Isotopes*, *27*(9), 515–525. https://doi.org/10.1016/0020-708x(76)90082-x

DeVries, T., & Holzer, M. (2019). Radiocarbon and helium isotope constraints on deep-ocean ventilation and mantle-^{3}He sources. *Journal of Geophysical Research: Oceans*, *124*(5), 3036–3057. https://doi.org/10.1029/2018jc014716

Edmond, J. M., Measures, C., McDuff, R. E., Chan, L. H., Collier, R. W., Grant, B., et al. (1979). Ridge crest hydrothermal activity and the balances of the major and minor elements in the ocean: The Galapagos data. *Earth and Planetary Science Letters*, *46*(1), 1–18. https://doi.org/10.1016/0012-821x(79)90061-x

Elderfield, H., & Schultz, A. (1996). Mid-ocean ridge hydrothermal fluxes and the chemical composition of the ocean. *Annual Review of Earth and Planetary Sciences*, *24*(1), 191–224. https://doi.org/10.1146/annurev.earth.24.1.191

Emerson, S., Ito, T., & Hamme, R. C. (2012). Argon supersaturation indicates low decadal-scale vertical mixing in the ocean thermocline. *Geophysical Research Letters*, *39*, L18610. https://doi.org/10.1029/2012GL053054

Gade, H. G. (1993). When ice melts in sea water: A review. *Atmosphere-Ocean*, *31*(1), 139–165. https://doi.org/10.1080/07055900.1993.9649466

Gebbie, G., & Huybers, P. (2010). Total matrix intercomparison: A method for determining the geometry of water mass pathways. *Journal of Physical Oceanography*, *40*(8), 1710–1728. https://doi.org/10.1175/2010jpo4272.1

Gebbie, G., & Huybers, P. (2012). The mean age of ocean waters inferred from radiocarbon observations: Sensitivity to surface sources and accounting for mixing histories. *Journal of Physical Oceanography*, *42*(2), 291–305. https://doi.org/10.1175/jpo-d-11-043.1

Gong, D. Y., & Wang, S. W. (1999). Definition of Antarctic oscillation index. *Geophysical Research Letters*, *26*(4), 459–462. https://doi.org/10.1029/1999gl900003

Gordon, A. L. (2019). Bottom water formation. In J. K. Cochran, J. H. Bokuniewicz, & L. P. Yager (Eds.), *Encyclopedia of ocean sciences* (pp. 120–126). Elsevier.

Gordon, A. L., Visbeck, M., & Comiso, J. C. (2007). A possible link between the Weddell Polynya and the Southern Annular Mode. *Journal of Climate*, *20*(11), 2558–2571. https://doi.org/10.1175/jcli4046.1

Gow, A. J., & Williamson, T. (1975). Gas inclusions in the Antarctic ice sheet and their glaciological significance. *Journal of Geophysical Research*, *80*(36), 5101–5108. https://doi.org/10.1029/jc080i036p05101

Hamme, R. C., Nicholson, D., Jenkins, W. J., & Emerson, S. R. (2019). Using noble gases to assess the ocean's carbon pumps. *Annual Review of Marine Science*, *11*(1), 75–103. https://doi.org/10.1146/annurev-marine-121916-063604

Hamme, R. C., & Severinghaus, J. P. (2007). Trace gas disequilibria during deep-water formation. *Deep-Sea Research I*, *54*(6), 939–950. https://doi.org/10.1016/j.dsr.2007.03.008

Hautala, S. L. (2018). The abyssal and deep circulation of the Northeast Pacific Basin. *Progress in Oceanography*, *160*, 68–82. https://doi.org/10.1016/j.pocean.2017.11.011

Hautala, S. L., & Hammond, D. E. (2020). Abyssal pathways and the double silica maximum in the Northeast Pacific Basin. *Geophysical Research Letters*, *47*(19), e2020GL089010. https://doi.org/10.1029/2020gl089010

Hellmer, H. H. (2004). Impact of Antarctic ice shelf basal melting on sea ice and deep ocean properties. *Journal of Geophysical Research*, *31*, L10307. https://doi.org/10.1029/2004GL019506

Henry, W. (1803). Experiments on the quantity of gases adsorbed by water, at different temperatures, and under different pressures. *Philosophical Transactions of the Royal Society (London)*, *93*(29–42), 274–276.

Hohmann, R., Schlosser, P., Jacobs, S., Ludin, A., & Weppernig, R. (2002). Excess helium and neon in the southeast Pacific: Tracers for glacial meltwater. *Journal of Geophysical Research*, *107*(C11), 3198. https://doi.org/10.1029/2000jc000378

Holland, P. R., Jenkins, A., & Holland, D. M. (2008). The response of ice shelf basal melting to variations in ocean temperature. *Journal of Climate*, *21*(11), 2558–2572. https://doi.org/10.1175/2007jcli1909.1

Holzer, M., DeVries, T., & de Lavergne, F. (2021). Diffusion controls the ventilation of a Pacific Shadow Zone above abyssal overturning. *Nature Communications*, *12*(4348), 4348. https://doi.org/10.1038/s41467-41021-24648-x

Huhn, O., Hellmer, H. H., Rhein, M., Rodehacke, C. B., Roether, W., Schodlock, M. P., & Shroder, M. (2008). Evidence of deep- and bottom-water formation in the western Weddell Sea. *Deep-Sea Research II*, *55*(8–9), 1098–1116. https://doi.org/10.1016/j.dsr2.2007.12.015

Ito, T., & Deutsch, C. (2006). Understanding the saturation state of argon in the thermocline: The role of air-sea gas exchange and diapycnal mixing. *Global Biogeochemical Cycles*, *20*, GB3019. https://doi.org/10.1029/2005GB002655

Ito, T., Deutsch, C., Emerson, S., & Hamme, R. C. (2007). Impact of diapycnal mixing on the saturation state of argon in the subtropical North Pacific. *Geophysical Research Letters*, *34*(9), L09602. https://doi.org/10.1029/2006GL029209

Jackett, D. R., & McDougall, T. J. (1997). A neutral density variable for the world's oceans. *Journal of Physical Oceanography*, *27*(2), 237–263. https://doi.org/10.1175/1520-0485(1997)027<0237:andvft>2.0.co;2

Jacobs, S. S., Hellmer, H. H., Doake, C. S. M., Jenkins, A., & Frolich, R. M. (1992). Melting of ice shelves and the mass balance of Antarctica. *Journal of Glaciology*, *38*(130), 375–387. https://doi.org/10.1017/s0022143000002252

Jacobs, S. S., Hellmer, H. H., & Jenkins, A. (1996). Antarctic ice sheet melting in the Southeast Pacific. *Geophysical Research Letters*, *23*(9), 957–960. https://doi.org/10.1029/96gl00723

Jenkins, W. J. (1980). Tritium and ^{3}He in the Sargasso Sea. *Journal of Marine Research*, *38*, 533–569.

Jenkins, W. J. (1988). *The use of anthropogenic tritium and ^{3}He to study subtropical gyre ventilation and circulation* (Vol. A325, pp. 43–61). Philosophical Transactions of the Royal Society (London).

Jenkins, W. J. (2020). Using excess ^{3}He to estimate southern ocean upwelling timescales. *Geophysical Research Letters*, *47*(15), e2020GL087266. https://doi.org/10.1029/2020gl087266

Jenkins, W. J., Doney, S. C., Fendrock, M., Fine, R., Gamo, T., Jean-Baptiste, P., et al. (2019). A comprehensive global oceanic dataset of helium isotope and tritium measurements. *Earth System Science Data*, *11*(2), 441–454. https://doi.org/10.5194/essd-11-441-2019

Jenkins, W. J., Doney, S. C., Seltzer, A. M., German, C. R., Lott, D. E. I., & Cahill, K. L. (2023). *A North Pacific meridional section (U.S. GEOTRACES GP15) of helium isotopes and noble gases II: Shallow distributions and tritium.* Global Biogeochemical Cycles. Submitted.

Jenkins, W. J., Edmond, J. M., & Corliss, J. B. (1978). Excess ^{3}He and ^{4}He in Galapagos submarine hydrothermal waters. *Nature*, *272*(5649), 156–158. https://doi.org/10.1038/272156a0

Jenkins, W. J., & German, C. R. (2021a). Helium isotope with helium and neon concentration data from Leg 1 (Seattle, WA to Hilo, HI) of the US GEOTRACES Pacific meridional transect (PMT) cruise (GP15, RR1814) on R/V Roger Revelle from September to October 2018. Biological and chemical Oceanography data management Office (BCO-DMO). (Version 1). In *BCO-DMO repository*, https://doi.org/10.26008/21912/bco-dmo.862182.862181

Jenkins, W. J., & German, C. R. (2021b). Helium isotope with helium and neon concentration data from Leg 2 (Hilo, HI to Papeete, French Polynesia) of the US GEOTRACES Pacific meridional transect (PMT) cruise (GP15, RR1815) on R/V Roger Revelle from Oct-Nov 2018. Biological and chemical Oceanography data management Office (BCO-DMO). (Version 1). In *BCO-DMO repository*, https://doi.org/10.26008/21912/bco-dmo.862220.862221

Jenkins, W. J., German, C. R., & Lott, D. E. I. (2022a). In W. J. Jenkins & D. E. I. Lott (Eds.), *GP15 heavy noble gas concentrations Leg 1*. BCO-DMO.

Jenkins, W. J., German, C. R., & Lott, D. E. I. (2022b). In W. J. Jenkins & D. E. I. Lott (Eds.), *GP15 heavy noble gas concentrations Leg 2*. BCO-DMO.

Jenkins, W. J., Hatta, M., Fitzsimmons, J., Schlitzer, R., Lanning, N., Shiller, A., et al. (2020). An intermediate-depth source of hydrothermal He-3 and dissolved iron in the North Pacific. *Earth and Planetary Science Letters*, *539*, 116223. https://doi.org/10.1016/j.epsl.2020.116223

Jenkins, W. J., Lott, D. E., III, & Cahill, K. L. (2019). A determination of atmospheric helium, neon, argon, krypton, and xenon solubility concentrations in water and seawater. *Marine Chemistry*, *211*(1), 94–107. https://doi.org/10.1016/j.marchem.2019.03.007

Jenkins, W. J., Lott, D. E., III, German, C. R., Cahill, K. L., Goudreau, J., & Longworth, B. E. (2018). The deep distributions of helium isotopes, radiocarbon, and noble gases along the U.S. GEOTRACES East Pacific zonal transect (GP16). *Marine Chemistry*, *201*(1), 167–182. https://doi.org/10.1016/j.marchem.2017.03.009

Jenkins, W. J., Lott, D. E., III, Longworth, B. E., Curtice, J. M., & Cahill, K. L. (2015). The distributions of helium isotopes and tritium along the U.S. GEOTRACES North Atlantic Sections (GEOTRACES GA03). *Deep Sea Research Part II: Topical Studies in Oceanography*, *116*(1), 21–28. https://doi.org/10.1016/j.dsr2.2014.11.017

Jenkins, W. J., Seltzer, A. M., Gebbie, G., & German, C. R. (2023). Deep Pacific evidence for a strengthening circumpolar trough over the past two millennia. *Nature Geoscience*.

Joyce, T. M., Warren, B. A., & Talley, L. D. (1986). The geothermal heating of the abyssal sub-Arctic Pacific-Ocean. *Deep-Sea Research, Part A: Oceanographic Research Papers*, *33*(8), 1003–1015. https://doi.org/10.1016/0198-0149(86)90026-9

Jullion, L., Garabato, A. C. N., Bacon, S., Meredith, M. P., Brown, P. J., Torres-Valdés, S., et al. (2014). The contribution of the Weddell Gyre to the lower limb of the Global Overturning Circulation. *Journal of Geophysical Research: Oceans*, *119*(6), 3357–3377. https://doi.org/10.1002/2013jc009725

Kato, F., & Kawabe, M. (2009). Volume transport and distribution of deep circulation at 165 degrees W in the North Pacific. *Deep-Sea Research Part I Oceanographic Research Papers*, *56*(12), 2077–2087. https://doi.org/10.1016/j.dsr.2009.08.004

Khatiwala, S. (2007). A computational framework for simulation of biogeochemical tracers in the ocean. *Global Biogeochemical Cycles*, *21*, GB3001. https://doi.org/10.1029/2007GB002923

Komaki, K., & Kawabe, M. (2009). Deep-circulation current through the Main Gap of the Emperor Seamounts Chain in the North Pacific. *Deep-Sea Research Part I Oceanographic Research Papers*, *56*(3), 305–313. https://doi.org/10.1016/j.dsr.2008.10.006

Kuhlbrodt, T., Griesel, A., Montoya, M., Levemann, A., Hofmann, M., & Rahmstorf, S. (2007). On the driving processes of the Atlantic meridional overturning circulation. *Reviews of Geophysics*, *45*, RG2001. https://doi.org/10.1029/2004RG000166

Kunze, E. (2017). Internal-wave-driven mixing: Global geography and budgets. *Journal of Physical Oceanography*, *47*(6), 1325–1345. https://doi.org/10.1175/jpo-d-16-0141.1

Kurz, M. D., & Jenkins, W. J. (2019). Volcanic helium. In J. K. Cochran, J. H. Bokuniewicz, & L. P. Yager (Eds.), *Encyclopedia of ocean sciences* (3rd ed., pp. 392–400). Elsevier.

Kurz, M. D., & Jenkins, W. J. (1981). The distribution of helium in oceanic basalt glasses. *Earth and Planetary Science Letters*, *53*(1), 41–54. https://doi.org/10.1016/0012-821x(81)90024-8

Kurz, M. D., Jenkins, W. J., & Hart, S. R. (1982). Helium isotopic systematics of oceanic islands and mantle heterogeneity. *Nature*, *297*(5861), 43–47. https://doi.org/10.1038/297043a0

Kurz, M. D., Moreira, M., Curtice, J., Lott, D., III, Mahoney, J., & Sinton, J. M. (2005). Correlated helium, neon, and melt production on the superfast spreading East Pacific Rise near 17S. *Earth and Planetary Science Letters*, *232*(1–2), 125–142. https://doi.org/10.1016/j.epsl.2005.01.005

Liang, J.-H., Deutsch, C., McWilliams, J. C., Baschek, B., Sullivan, P. P., & Chiba, D. (2013). Parameterizing bubble-mediated air-sea gas exchange and its effect on ocean ventilation. *Global Biogeochemical Cycles*, *27*(3), 894–905. https://doi.org/10.1002/gbc.20080

Loose, B., & Jenkins, W. J. (2014). The five stable noble gases are sensitive and unambiguous tracers of glacial meltwater. *Geophysical Research Letters*, *41*(8), 2835–2841. https://doi.org/10.1002/2013gl058804

Loose, B., Jenkins, W. J., Moriarty, R., Brown, P., Jullion, L., Naveira Garabato, A. C., et al. (2016). Estimating the recharge properties of the deep ocean using noble gases and helium isotopes. *Journal of Geophysical Research: Oceans*, *121*(8), 5959–5979. https://doi.org/10.1002/2016jc011809

Lupton, J. E. (1998a). Hydrothermal helium plumes in the Pacific Ocean. *Journal of Geophysical Research*, *103*(C8), 15853–15868. https://doi.org/10.1029/98jc00146

Lupton, J. E. (1998b). Water column hydrothermal plumes on the Juan de Fuca Ridge. *Journal of Geophysical Research*, *95*(B8), 12829–12842. https://doi.org/10.1029/jb095ib08p12829

Lupton, J. E., Baker, E. T., & Massoth, G. J. (1999). Helium, heat, and the the generation of hydrothermal event plumes at mid-ocean ridges. *Earth and Planetary Science Letters*, *171*(3), 343–350. https://doi.org/10.1016/s0012-821x(99)00149-1

Lupton, J. E., & Craig, H. (1981). A major helium-3 source at 15S on the East Pacific Rise. *Science*, *214*(4516), 13–18. https://doi.org/10.1126/science.214.4516.13

MacDonald, A. M., Mecking, S., Robbins, P. E., Toole, J. M., Johnson, G. C., Talley, L., et al. (2009). The WOCE-era 3-D Pacific Ocean circulation and heat budget. *Progress in Oceanography*, *82*(4), 281–325. https://doi.org/10.1016/j.pocean.2009.08.002

Mengis, N., Keller, D. P., MacDougall, A. H., Eby, M., Wright, N., Meissner, K. J., et al. (2020). Evaluation of the University of Victoria Earth System Climate Model version 2.10 (UVic ESCM 2.10). *Geoscientific Model Development*, *13*(9), 4183–4204. https://doi.org/10.5194/gmd-13-4183-2020

Meredith, M., & Hogg, A. M. (2006). Circumpolar response of Southern Ocean eddy activity to a change in the Southern Annular Mode. *Geophysical Research Letters*, *33*, L16608. https://doi.org/10.1029/2006GL026499

Moore, J. C., & Vrolijk, P. (1992). Fluids in accretionary prisms. *Reviews of Geophysics*, *30*(2), 113–135. https://doi.org/10.1029/92rg00201

Morrison, P., & Pine, J. (1955). Radiogenic origin of helium isotopes in rock. *Annals of the New York Academy of Sciences*, *62*(3), 69–92.

Munk, W. H. (1966). Abyssal recipes. *Deep-Sea Research*, *13*(4), 707–730. https://doi.org/10.1016/0011-7471(66)90602-4

Nicholson, D. P., Khatiwala, S., & Heimbach, P. (2016). Noble gas tracers of ventilation during deep-water formation in the Weddell Sea. *IOP Conference Series: Earth and Environmental Science*, *35*, 012019. https://doi.org/10.1088/1755-1315/1035/1081/012019

Orr, J. C., Najjar, R. G., Aumont, O., Bopp, L., Bullister, J. L., Danabasoglu, G., et al. (2017). Biogeochemical protocols and diagnostics for the CMIP6 Ocean Model Intercomparison Project (OMIP). *Geoscientific Model Development*, *10*(6), 2169–2199. https://doi.org/10.5194/gmd-10-2169-2017

Orsi, A. H., Jacobs, S. S., Gordon, A. L., & Visbeck, M. (2001). Cooling and ventilating the abyssal ocean. *Geophysical Research Letters*, *28*(15), 2923–2926. https://doi.org/10.1029/2001gl012830

Orsi, A. H., Smethie, W. M., & Bullister, J. L. (2002). On the total input of Antarctic waters to the deep ocean: A preliminary estimate from chlorofluorocarbon measurements. *Journal of Geophysical Research*, *107*(C8), 3122. https://doi.org/10.1029/2001jc000976

Owens, W. B., & Warren, B. A. (2001). Deep circulation in the northwest corner of the Pacific Ocean. *Deep-Sea Research Part I Oceanographic Research Papers*, *48*(12), 2727. https://doi.org/10.1016/s0967-0637(01)00028-0

Reid, J. L. (1997). On the total geostrophic circulation of the Pacific Ocean: Flow patterns, tracers, and transports. *Progress in Oceanography*, *39*(4), 263–352.

Resing, J. A., Sedwick, P. N., German, C. R., Jenkins, W. J., Moffett, J. W., Sohst, B. M., & Tagliabue, A. (2015). Basin-Scale transport of hydrothermal dissolved metals across the South Pacific Ocean. *Nature*, *523*(7559), 203–206. https://doi.org/10.1038/nature14577

Rhodes, R. H., Bertler, N. A. N., Baker, J. A., Steen-Larsen, H. C., Sneed, S. B., Morgenstern, U., & Johnsen, S. J. (2012). Little Ice Age climate and oceanic conditions of the Ross Sea, Antarctica from a coastal ice core record. *Climate of the Past*, *8*(4), 1223–1238. https://doi.org/10.5194/cp-8-1223-2012

Rignot, E., Jacobs, S., Mouginot, J., & Scheuchl, B. (2013). Ice-shelf melting around Antarctica. *Science*, *341*(6143), 266–270. https://doi.org/10.1126/science.1235798

Sayles, F. L., & Jenkins, W. J. (1982). Advection of pore fluids through sediments in the equatorial East Pacific. *Science*, *217*(4556), 245–248. https://doi.org/10.1126/science.217.4556.245

Schlitzer, R. (2016). Quantifying He fluxes from the mantle using multi-tracer data assimilation. *Philosophical Transactions of the Royal Society A: Mathematical, Physical and Engineering Sciences*, *374*(2081), 20150288. https://doi.org/10.1098/rsta.2015.0288

Schlosser, E., Powers, J. G., Duda, M. G., & Manning, K. W. (2011). Interaction between Antarctic sea ice and synoptic activity in the circumpolar trough: Implications for ice-core interpretation. *Annals of Glaciology*, *52*(57), 9–17. https://doi.org/10.3189/172756411795931859

Seltzer, A. M., Nicholson, D. P., Smethie, W. M., Tyne, R. L., Le Roy, E., Stanley, R. H. R., et al. (2023). Dissolved gases in the deep North Atlantic track ocean ventilation processes. *Proceedings of the National Academy of Sciences of the United States of America*, *120*(11), e2217946120. https://doi.org/10.1073/pnas.2217946120

Simms, A. R., Bentley, M. J., Simkins, L. M., Zurbuchen, J., Reynolds, L. C., DeWitt, R., & Thomas, E. R. (2021). Evidence for a "Little Ice Age" glacial advance within the Antarctic Peninsula—Examples from glacially-overrun raised beaches. *Quaternary Science Reviews*, *271*, 107195. https://doi.org/10.1016/j.quascirev.2021.107195

Stanley, R. H. R., Baschek, B., Lott, D. E., III, & Jenkins, W. J. (2009). A new automated method for measuring noble gases and their isotopic ratios in water samples. *Geochemistry, Geophysics, Geosystems*, *10*(5), Q05008. https://doi.org/10.01029/02009GC002429

Stanley, R. H. R., Jenkins, W. J., Lott, D. E., III, & Doney, S. C. (2009). Noble gas constraints on air-sea gas exchange and bubble fluxes. *Journal of Geophysical Research*, *114*, C11020. https://doi.org/10.1029/2009JC005396

Stark, S., Jenkins, W. J., & Doney, S. C. (2004). Deposition and recirculation of tritium in the North Pacific Ocean. *Journal of Geophysical Research*, *109*, C06099. https://doi.org/10.1029/2003JC002150

Stommel, H. (1982). Is the South Pacific helium-3 plume dynamically active? *Earth and Planetary Science Letters*, *61*(1), 63–67. https://doi.org/10.1016/0012-821x(82)90038-3

Straume, E. O., Gaina, C., Medvedev, S., Hochmuth, K., Gohl, K., Whittaker, J. M., et al. (2019). GlobSed: Updated total sediment thickness in the world's oceans. *Geochemistry, Geophysics, Geosystems*, *20*(4), 1756–1772. https://doi.org/10.1029/2018gc008115

Suess, E., Bohrmann, G., von Huene, R., Linke, P., Wallmann, K., Lammers, S., et al. (1998). Fluid venting in the eastern Aleutian subduction zone. *J Geophys ResSolid Earth*, *103*(B2), 2597–2614. https://doi.org/10.1029/97jb02131

Talley, L. D. (2013). Closure of the global overturning circulation through the Indian, Pacific, and southern oceans: Schematics and transports. *Oceanography*, *26*(1), 80–97. https://doi.org/10.5670/oceanog.2013.07

von Huene, R., Klaeschen, D., Gutscher, M., & Fruehn, J. (1998). Mass and fluid flux during accretion at the Alaskan margin. *Geological Society of America Bulletin*, *110*(4), 468–482. https://doi.org/10.1130/0016-7606(1998)110<0468:maffda>2.3.co;2

Well, R., Lupton, J. E., & Roether, W. (2001). Crustal helium in deep Pacific Waters. *Journal of Geophysical Research*, *106*(C7), 14165–14177. https://doi.org/10.1029/1999jc000279

Wijffels, S. E., Toole, J. M., Bryden, H. L., Fine, R. A., Jenkins, W. J., & Bullister, J. L. (1996). The water masses and circulation at 10°N in the Pacific. *Deep-Sea Research I*, *43*(4), 501–544. https://doi.org/10.1016/0967-0637(96)00006-4

Wijffels, S. E., Toole, J. M., & Davis, R. E. (2001). Revisiting the South Pacific subtropical circulation: A synthesis of WOCE observations along 32S. *Journal of Geophysical Research*, *106*(C9), 19481–19513. https://doi.org/10.1029/1999jc000118

Young, C., & Lupton, J. E. (1983). An ultratight fluid sampling system using cold-welded copper tubing. *EOS Transactions AGU*, *64*, 735.

Zheng, Y., Heywood, K. J., Webber, B. G. M., Stevens, D. P., Biddle, L. C., Boehme, L., & Loose, B. (2021). Winter seal-based observations reveal glacial meltwater surfacing in the southeastern Amundsen Sea. *Communications Earth & Environment*, *2*(1), 40. https://doi.org/10.1038/s43247-021-00111-z